

©2018. American Geophysical Union. All Rights Reserved

Kinne, Stefan, Declan O'Donnel, Philip Stier, Silvia Kloster, Kai Zhang, Hauke Schmidt, Sebastian Rast, Marco Giorgetta, Tom F. Eck, and Bjorn Stevens. "MAC-v1: A New Global Aerosol Climatology for Climate Studies." *Journal of Advances in Modeling Earth Systems* 5, no. 4 (2013): 704–40.

<https://doi.org/10.1002/jame.20035>. || <https://doi.org/10.1002/jame.20035>

This item is likely protected under Title 17 of the U.S. Copyright Law. Unless on a Creative Commons license, for uses protected by Copyright Law, contact the copyright holder or the author.

Access to this work was provided by the University of Maryland, Baltimore County (UMBC) ScholarWorks@UMBC digital repository on the Maryland Shared Open Access (MD-SOAR) platform.

Please provide feedback

Please support the ScholarWorks@UMBC repository by emailing scholarworks-group@umbc.edu and telling us what having access to this work means to you and why it's important to you. Thank you.

MAC-v1: A new global aerosol climatology for climate studies

Stefan Kinne,¹ Declan O'Donnel,² Philip Stier,³ Silvia Kloster,¹ Kai Zhang,^{1,4} Hauke Schmidt,¹ Sebastian Rast,¹ Marco Giorgetta,¹ Tom F. Eck,^{5,6} and Bjorn Stevens¹

Received 21 August 2012; revised 6 June 2013; accepted 10 June 2013; published 4 October 2013.

[1] The Max-Planck-Institute Aerosol Climatology version 1 (MAC-v1) is introduced. It describes the optical properties of tropospheric aerosols on monthly timescales and with global coverage at a spatial resolution of 1° in latitude and longitude. By providing aerosol radiative properties for any wavelength of the solar (or shortwave) and of the terrestrial (or longwave) radiation spectrum, as needed in radiative transfer applications, this MAC-v1 data set lends itself to simplified and computationally efficient representations of tropospheric aerosol in climate studies. Estimates of aerosol radiative properties are provided for both total and anthropogenic aerosol in annual time steps from preindustrial times (i.e., starting with year 1860) well into the future (until the year 2100). Central to the aerosol climatology is the merging of monthly statistics of aerosol optical properties for current (year 2000) conditions. Hereby locally sparse but trusted high-quality data by ground-based sun-photometer networks are merged onto complete background maps defined by central data from global modeling with complex aerosol modules. This merging yields 0.13 for the global annual midvisible aerosol optical depth (AOD), with 0.07 attributed to aerosol sizes larger than $1\ \mu\text{m}$ in diameter and 0.06 of attributed to aerosol sizes smaller than $1\ \mu\text{m}$ in diameter. Hereby larger particles are less absorbing with a single scattering albedo (SSA) of 0.98 compared to 0.93 for smaller sizes. Simulation results of a global model are applied to prescribe the vertical distribution and to estimate anthropogenic contributions to the smaller size AOD as a function of time, with a 0.037 value for current conditions. In a demonstration application, the associated aerosol direct radiative effects are determined. For current conditions, total aerosol is estimated to reduce the combined shortwave and longwave net-flux balance at the top of the atmosphere by about $-1.6\ \text{W/m}^2$ from which $-0.5\ \text{W/m}^2$ (with an uncertainty of $\pm 0.2\ \text{W/m}^2$) is attributed to anthropogenic activities. Based on past and projected aerosol emission data, the global anthropogenic direct aerosol impact (i.e., ToA cooling) is currently near the maximum and is projected to drop by 2100 to about $-0.3\ \text{W/m}^2$. The reported global averages are driven by considerable spatial and temporal variability. To better convey this diversity, regional and seasonal distributions of aerosol optical properties and their radiative effects are presented. On regional scales, the anthropogenic direct aerosol forcing can be an order of magnitude stronger than the global average and it can be of either sign. It is also shown that maximum anthropogenic impacts have shifted during the last 30 years from the U.S. and Europe to eastern and southern Asia.

¹Atmosphere in the Earth System, Max Planck Institute for Meteorology, Hamburg, Germany.

²Climate Change Research, Finnish Meteorological Institute, Helsinki, Finland.

³Department of Physics, University of Oxford, Oxford, UK.

⁴Department of Climate Physics, Pacific North National Laboratory, Richland, Washington, USA.

⁵Biospheric Sciences Laboratory, NASA Goddard Space Flight Center, Greenbelt, Maryland, USA.

⁶GESTAR, Universities Space Research Association, Columbia, Maryland, USA.

Corresponding author: S. Kinne, Max Planck Institute for Meteorology, Bundesstr. 53, Hamburg DE-20146, Germany. (stefan.kinne@zmaw.de)

Citation: Kinne, S., D. O'Donnel, P. Stier, S. Kloster, K. Zhang, H. Schmidt, S. Rast, M. Giorgetta, T. F. Eck, and B. Stevens (2013), MAC-v1: A new global aerosol climatology for climate studies, *J. Adv. Model. Earth Syst.*, 5, 704–740, doi:10.1002/jame.20035.

1. Introduction

[2] Atmospheric aerosol is linked to large uncertainties in understanding climate change [*Intergovernmental Panel on Climate Change*, 2007]. Part of the problem can be attributed to an insufficiently accurate representation of the tropospheric aerosol, which is also highly variable in space and time. This is a result of relatively short tropospheric lifetimes (in the order of a few days)

in combination with a multitude of different aerosol sources. Thus, a proper representation needs to capture not only the variability in aerosol concentration but also the variability in aerosol composition and size. One way to describe this variability for tropospheric aerosol in global modeling is a detailed treatment of aerosol components and their processes in aerosol submodules that can be incorporated into Earth-System models. Unfortunately, the output of these aerosol modules is diverse, as many of the underlying processes are either unknown or can only be represented in simplistic ways. Even so, the complexity of such aerosol modules can be enormous with concomitant computational demands. However, for many climate processes, the coupling of aerosol processes to the climate system is not believed to play an important role. Thus, a simple description of the radiative properties of the aerosol can be very useful. An analogy is the albedo of land surfaces. The surface albedo has a large influence on the climate system. However, for most studies a climatology describing the characteristic optical properties of land surfaces including their spatial, spectral, and temporal variation appears sufficient compared to otherwise complex submodules that attempt to predict the albedo of the terrestrial biosphere from first principles. The development of such a simplifying description for the representation of tropospheric aerosol is the purpose of this contribution.

[3] There were previous efforts to represent global distributions of aerosol optical properties, most notably by a climatology developed by Didier Tanre in the mid-1980 [Tanre *et al.*, 1984] and the GADS climatology by Peter Köpke in the mid-1990 [Köpke *et al.*, 1997]. However, these aerosol climatologies have limitations. The Tanre climatology provides aerosol radiative properties for mixtures of maritime, continental, urban, desert, and background aerosol based on assumed geographical distributions. The Tanre climatology neglects seasonal variations and features a wide aerosol spot centered over the Saharan desert which is associated with a relatively strong absorption. The GADS climatology is one of the first attempts to represent a greater diversity in aerosol composition. Ten different aerosol types are predefined in terms of size, spectral refractive indices, and hygroscopicity. The GADS climatology defines global distributions for type mixture, amount, and ambient relative humidity, however only for 2 months (January and July). Hereby, type-mixture definitions refer to dry aerosol, as GADS is largely developed from in situ ground-based dried sample analyses. For the determination of ambient aerosol optical properties, this dry definition introduces extra uncertainties, because component dependent assumptions to water uptake are required (which are calculated with the Optical Properties of Aerosols and Clouds [OPAC] tool of Hess *et al.* [1998]). Another limitation is the coverage for just 2 months, which is inadequate to capture the seasonality. For instance, the maxima of biomass burning over southern Africa and southern America occur between August and November and are missed. The new aerosol climatology, named Max-Planck-Institute Aerosol Climatology version 1 (MAC-v1) as described in this contribution

attempts to address these shortcomings, by offering global maps at $1 \times 1^\circ$ (latitude/longitude) resolution for each month. Hereby, MAC-v1 takes advantage of recent developments in aerosol (global) modeling and observational capabilities for aerosol optical properties.

[4] During the last 15 years, extra efforts were made to capture and quantify the aerosol optical properties with aerosol dedicated measurements from ground and space. Ground networks of sun-/sky-photometer robots [Holben *et al.*, 1998; Aoki *et al.*, 2006] have been put in place to monitor at selected ground sites all relevant aerosol column optical properties. Measurements of the direct solar radiation at cloud-free conditions capture the attenuation due to aerosol with high accuracy. Hereby, solar subspectral attenuations are expressed by the vertically normalized aerosol optical depth (AOD). In addition to the direct solar attenuation measurements, less frequent sky-radiance samples permit inversion methods to derive size-distribution detail (for the 0.05–15 μm radius range) and data on aerosol absorption. At a few sites, colocated lidars [Welton *et al.*, 2001; Bösenberg *et al.*, 2003; Sugimoto *et al.*, 2008] add complementary data on the aerosol vertical distribution via aerosol backscatter profiles or aerosol extinction profiles. Despite the sparse and uneven distribution of these ground network data, local comparisons in reference to the accuracy and detail offered by sun-/sky-photometer statistics have led to more mature satellite retrievals by constraining required a priori assumptions and to reduced diversity for simulated AOD by complex aerosol modules in global modeling.

[5] During the last 15 years, many new passive satellite sensors were deployed with increased spectral, viewing or polarization capabilities better suited to extract aerosol properties (e.g., MODIS, MISR, Polarization and Anisotropy of Reflectances for Atmospheric science coupled with Observations from a Lidar [PARASOL], OMI, SeaWiFS, or ATSR). All these satellite retrievals offer global maps for the midvisible AOD. Despite a general agreement in seasonal AOD distribution patterns, there are often offsets and significant regional differences among data sets not only from different sensors, but even from data sets of the same sensor. These are not only caused by sampling differences but also by limitations to satellite sensor capabilities and by AOD retrieval assumptions. In contrast to sun-photometry, satellite remote sensing of aerosol is usually derived from (subspectral) changes to the solar reflectance. The applied methods require assumptions to the aerosol composition (size, absorption) and to signal contributions by the background (surface or underlying clouds). Composition is usually prescribed with respect to average conditions and, more critically, background contributions are often so uncertain, that few or no retrievals are offered over surfaces with higher solar reflection (snow, ice, desert, or glint). Nonetheless, satellite data provide useful information on spatial and temporal distribution patterns for aerosol, especially over regions where ground monitoring is sparse (developing countries) or not available (over many ocean regions).

[6] During the last 15 years, the treatment of aerosol in global modeling has advanced tremendously. In

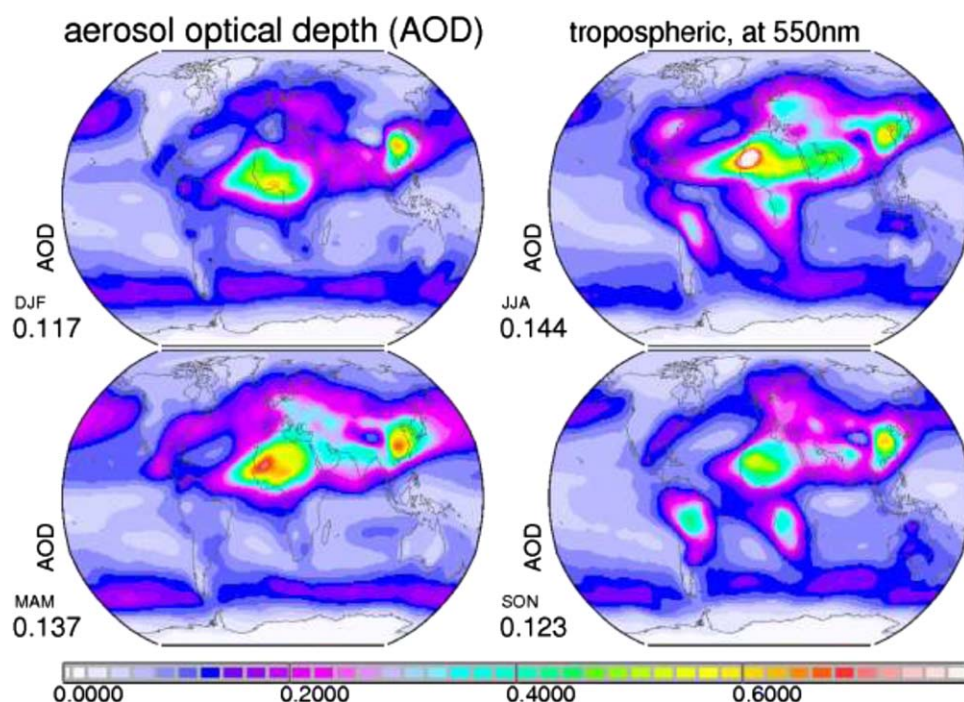


Figure 1. Seasonal average maps for the tropospheric midvisible AOD of the new MAC-v1 climatology for year 2000 conditions. Values below the labels indicate global averages.

pecially developed submodules aerosol particles are differentiated by both their size and composition [Kinne *et al.*, 2006]. Many existing processes have been improved and many new processes were added, including interactions with clouds (e.g., role of aerosol to serve as cloud nuclei), chemistry (e.g., phase transitions), and other aerosol types (e.g., internal mixing). To control the increasing degrees of freedom in modeling, as more processes are added to replace parameterizations, observational constraints are needed. These constraints exist in general only for highly integrated and interpreted model output (e.g., estimates for aerosol column optical properties or mass concentrations near the surface). While significant model diversity remains at subprocess modeling, which is also related to fundamental gaps in understanding, common features in global modeling can assist in extending observational samples in context and coverage (both in space and time). Examples include distributions of aerosol properties at night, aerosol properties in conjunction with clouds and aerosol properties over regions with few or no ground sites (e.g., dust outflow and biomass outflow off continents).

[7] The idea to create a more representative climatology for aerosol column optical properties with the recent advances in observational capabilities and more detail in modeling is not new. For instance in data assimilations, AOD data from satellite retrievals have been applied to correct model output toward observations. However, these studies are mainly applied for regional aerosol assessment studies [e.g., Collins *et al.*, 2001] or for short-term aerosol forecasts [e.g., Benedetti *et al.*, 2009] and usually are not applied over longer

time periods to address climatological aspects. Moreover, the satellite derived AOD retrievals are not error free and an improvement to AOD fields in model output often goes along with a worsening in aerosol composition, which is not constrained in the assimilation.

[8] In contrast to AOD data from satellite retrievals, sun/sky-photometers observations provide consistent and reliable data for all relevant aerosol column optical properties to represent average attenuation, size, and composition. Due to the data sparseness and the uneven global site distribution of ground sites, however, these photometer data are less suited for global data assimilations. Still, the combination of their monthly statistics to improve global aerosol products of satellite remote sensing and/or global modeling seems attractive. Most notable are two similar approaches [Liu *et al.*, 2005; Chung *et al.*, 2005]. However, both approaches are strongly tied to (less certain) AOD data from satellite remote sensing and to model output by only one particular global model (Goddard Chemistry Aerosol Radiation and Transport [GOCART] model) [Chin *et al.*, 2002].

[9] The MAC-v1 climatology, in contrast to these approaches, stays away from satellite (AOD) products and focuses more on details offered by sun/sky-photometry. In addition, when developing the MAC-v1 climatology (for aerosol column optical properties), an ensemble of model output is used, rather than relying on the output of a single model to bridge data gaps. Resulting global seasonal maps for the midvisible AOD and annual maps for different AOD subcomponents are presented in Figures 1 and 2, respectively.

[10] Beyond the explanation of methods for the derivation of global maps of aerosol column properties, this

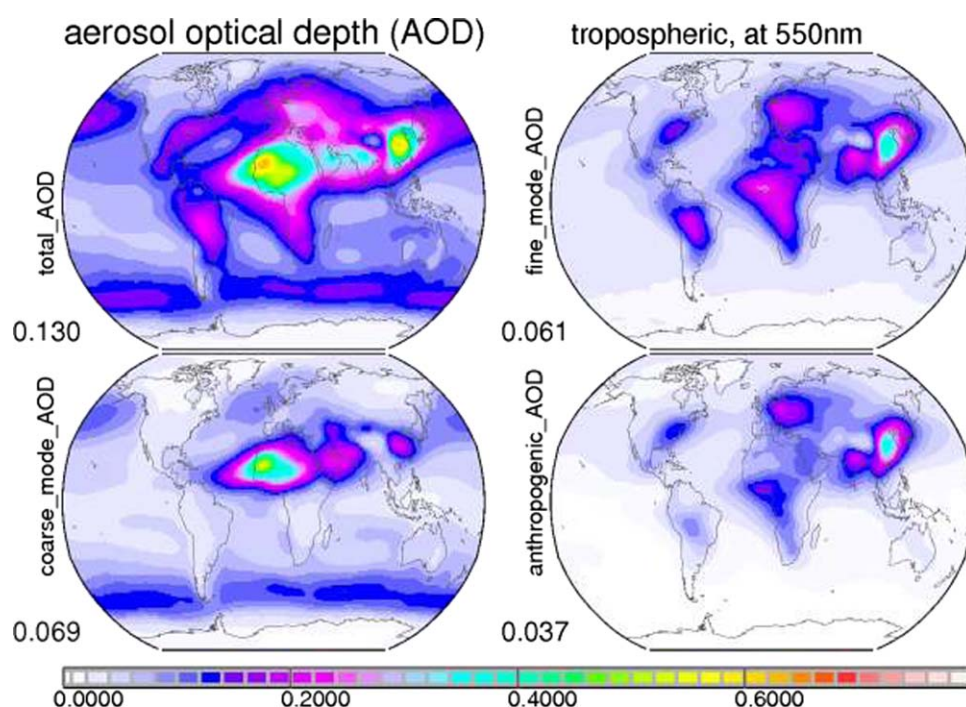


Figure 2. Annual average maps for the tropospheric midvisible AOD of the new climatology for current (year 2000) conditions. Aside from (top left) the total AOD also the separation into contributions (bottom left) by coarse-mode aerosol sizes and (top right) by fine-mode aerosol sizes are presented, as well as the estimate for (bottom right) anthropogenic AOD, as a fraction of the fine-mode AOD. Values below the labels indicate global (annual) averages.

contribution also explains an extension of these data with support from global modeling and observations so that broadband radiative transfer simulations can be performed. This includes a spectral extension, a vertical distribution and the consideration of temporal change via assumptions for anthropogenic aerosol. Subsequently, these data are fed into a radiative transfer code and global maps are derived that describe the direct radiative effects of total aerosol for the combined solar and infrared spectrum and for the solar spectrum. The main focus of this application, however, is on the direct climate forcing by anthropogenic aerosol, also as a function of time, and on aerosol forcing uncertainty.

[11] Section 2 outlines the development of the aerosol column optical properties for the reference year 2000. Section 3 explains methods and assumptions for the spectral expansion. Section 4 introduces the applied data for the vertical stratification. And section 5 quantifies anthropogenic AOD contribution as a function of time from the year 1850 to 2100. Now, with all the required aerosol input for radiative transfer simulations available, section 6 presents the associated aerosol direct radiative effects, including maps and averages for the aerosol direct (radiative) forcing. Section 7 adds sensitivity tests to address aerosol forcing uncertainty and a brief summary along with an outlook is given in section 8.

2. Aerosol Column Optical Properties

[12] Aerosol optical properties at the midvisible wavelength of 550 nm, vertically integrated over the

atmospheric column, for current (year 2000) conditions are the heart of the climatology. A central element of the MAC-v1 climatology is to establish global ($1 \times 1^\circ$ latitude/longitude) monthly maps in a data-merging process. Hereby, first guess background fields are regionally modified at and near locations, where higher quality data are available.

[13] First, relevant aerosol properties are briefly explained. Then, in preparation of a data-merging procedure, background data as well as trusted local data are introduced. Next, the merging procedure is illustrated and resulting global maps for the midvisible AOD. And finally, the resulting global maps and averages are compared to complementary data of similar efforts.

2.1. Optical Properties

[14] The merging process is applied to three midvisible (550 nm) aerosol column optical properties. The three properties are the aerosol optical depth (AOD), the single scattering albedo (SSA), or its twin, the absorption aerosol optical depth (AAOD) and the Angstrom parameter (AnP). AOD is the vertical normalized solar attenuation by atmospheric aerosol and represents the overall aerosol amount. SSA describes the probability of scattering in the context of both scattering and absorption processes to define the scattering potential. Alternatively, $1 - \text{SSA}$ defines the absorption potential. Multiplying by the AOD yields the absorption aerosol optical depth ($\text{AAOD} = [1 - \text{SSA}] \times \text{AOD}$) is an

absolute measure for aerosol absorption. AnP is a general indicator for aerosol size and is derived from the solar spectral dependence of the AOD. With AOD data at two or more midvisible solar wavelengths, AnP is defined by the negative slope in $\log(\text{AOD})/\log(\text{wavelength})$ space.

2.2. Background Data

[15] Background maps are based on data from global modeling. Modeling offers complete and consistent maps for AOD, SSA, and AnP. Background maps for these quantities are defined by model output of AeroCom 1 experiments. All models that participated in these experiments are global models with complex aerosol modules. In AeroCom 1 experiments models were forced by meteorological reanalysis data (e.g., temperature and wind) for the year 2000. In these models estimated emissions associated with current (year 2000) and preindustrial conditions (1750) for different aerosol types (e.g., soot, dust, sea salt, sulfate, and organics) and their precursors [Dentener *et al.*, 2006] were processed (involving assumptions for chemistry, mixing, transport, and removal) to yield global maps for aerosol burden [e.g., Textor *et al.*, 2006] and associated aerosol optical properties. Under the umbrella AeroCom initiative (<http://aerocom.met.no/Welcomes.html>) individual model output was compared to each other and to available data from remote sensing. It was found that model output agreed quite closely with the global annual average for AOD (which is rather well constrained by remote sensing), but diversity sharply increased for spatial AOD distributions and AOD-type attribution [Kinne *et al.*, 2006]. It was also demonstrated that for aerosol optical properties global maps of the ensemble mean performed better than those of any individual model. Thus, the modeling background maps for this MAC-v1 climatology are based on maps of local monthly ensemble median values available from global AeroCom phase 1 models (14 models for AOD, 11 for SSA, and 9 for AnP; for monthly global maps see Appendix of Kinne *et al.* [2006] with year 2000 emission data as model input [Dentener *et al.*, 2006]. Although during the last decade, in the context of ongoing AeroCom phase 2 efforts, many modeling groups improved physical and process detail (i.e., including nitrate as additional component, incorporating complex chemical schemes to treat secondary organics, allowing for internal component mixing or redefining water uptake schemes) the overall model performance with respect to optical properties did not vastly change and even did not always improve with the added complexity. Given, the advantage of more participating models in AeroCom phase 1 and the use of same emission and meteorological data for the same year as model input, ensemble data of AeroCom 1 were chosen as background maps.

2.3. Local Data

[16] Local data of high quality are offered by sun-/sky-photometer measurements. The most prominent ground network is the AEROSOL ROBOTIC NETWORK.

AERONET is a federation of ground-based remote sensing aerosol networks established in the mid-1990s by NASA and CNRS with further expansion through national agencies, universities, or individuals [Holben *et al.*, 1998]. With immediate data transfers via satellite or internet to a central data processing facility (at NASA-GSFC), associated aerosol column optical properties and derived aerosol column microphysical properties are available within hours via <http://aeronet.gsfc.nasa.gov/>. The main products are AOD (at accuracies better than 0.01) [Eck *et al.*, 1999] and AnP from direct solar attenuation (AERONET version 2, level 2.0) measurements. In addition, sky radiance samples (AERONET version 2, level 2.0, with removed refractive indices recovered from AERONET version 2, level 1.5) in combination with the direct solar attenuation data allow via an inversion method [Dubovik and King, 2000] to extract detail on size-distribution data and data for spectrally dependent refractive indices. Via the imaginary parts of these indices the overall aerosol absorption is described. However, as the retrieved absorption, which defines the SSA, is based on reductions to solar diffuse scattering, the absorption data are less accurate at lower AOD values and for lower air-mass factors of higher sun elevations [Dubovik *et al.*, 2000]. To reduce SSA uncertainty, only samples of sun-elevations below 45° are considered and SSA values associated with AOD values lower than 0.3 (in the midvisible spectral region) are assigned SSA values that are associated with stronger or the strongest AOD during that month at each site. Available AERONET data between 1996 and 2008 from more than 300 sites worldwide are combined into local multiannual monthly averages.

2.4. Local Data Gridding

[17] The concept of improving background data with local samples of higher quality requires the identifications of spatial matches. To do so, local (AERONET) data are combined onto the regular grid of the background model (here, $1^\circ \times 1^\circ$ in latitude/longitude). This combination considered that individual AERONET sites supplied data different in quality and different in their ability to represent the surrounding region. Each AERONET site is assigned a range score (3, 2, 1, 0) and a quality score (3, 2, 1, 0). Both scores were subjectively assigned (T. Eck, 2009, personal communication) by the AERONET staff at NASA-GSFC, which regularly examines data quality and is involved in the instrument deployment. Range and quality scores for AERONET sites with better seasonal coverage are listed in Appendix B.

[18] The range score captures the ability of local statistics to represent properties beyond the local grid region. A score of 0 indicates that site statistics is confined to the home grid cell. Range scores of 1, 2, or 3 indicate that statistics of the corresponding site has increased application domains of 3×3 , 5×5 , or 9×9 1° grid boxes, corresponding to 300, 500, and 900 km at the equator, respectively. Thus, any time the range score of a site exceeds zero, its statistics also serves as reference for neighboring grid points. This

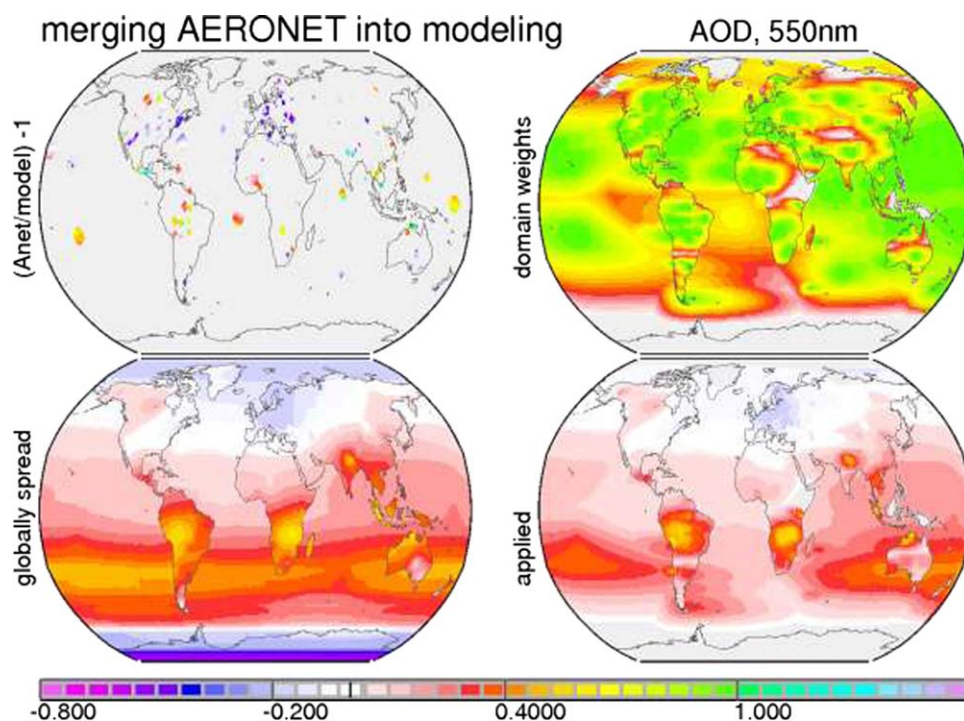


Figure 3. Illustration of substeps for the merging local (AERONET) statistics on background maps (by modeling) for the example of the annual AOD. (top right) Except for the site domain weights which vary between 0 and 1, all other maps indicate correction factors with respect to the background minus 1: Positive data indicate a required increase and negative data require a decrease. (top left) After identifying adjustment factors (step 1) at matching locations, (bottom right) these factors are globally stretched (step 2) to yield an adjustment factor map. (top right) Values of the factor maps are locally multiplied with the domain weight to yield the applied adjustment factors (step 3). As demonstrated for the annual AOD in this, for example of AOD in this figure, the applied corrections increase the AOD almost everywhere except over Europe and increases are strongest over (sub) tropical biomass burning regions.

automatically increases the number of matches to background data and elevates the importance of sites with higher spatial range scores. It is noted that in reality a range score can vary by season, especially when aerosol composition changes during the annual cycle. However, in this analysis a simplified approach assigns only the range score of the season with the highest aerosol loading for the entire year.

[19] The quality score indicates the general accuracy of the data and their usefulness. A quality score of 3 indicates data excellence and assigns a quality weight of 1.00. Scores of 2 and 1 with reduced quality weights of 0.67 and 0.33 reflect problems related to either the instrument (operational, maintenance, and sensor issues) or location (a complex local orographic environment limits an application to a coarse horizontal resolution). Sites with a quality score of zero are ignored. Into this category also fall high-altitude mountain sites, because they are unable to represent even the smallest spatial scales (100×100 km) considered here.

[20] Site scores are important to the determination of the local data, when several sites influence the same local geographic region. In that case the characteristic value for a grid region is represented by a weighted average. The applied weights of individual sites are a function of their quality weight and their range score. Hereby, for a

site with a better (than zero) range score, its quality weight is extended to surrounding grid points at a reduced level with distance from the original grid location (0.5, 0.2, 0.1, and 0.06 for the first, second, third, and fourth layer, see also Figure B1 in Appendix B). For a range score of 1 only the first directly surrounding grid squares are involved. Two rings of squares are affected for range score of 2 and all four surrounding squares are assigned such distance reduced weights for a range score of 3. Once all sites are processed at each grid point, the weighted average of all contributions defines the local grid value. Again, by allowing selected sites to represent also their surrounding grid regions the number of reference grid regions is significantly increased.

2.5. Data Merging

[21] The locally trusted monthly statistics (of AERONET) is merged onto the background data (of global modeling). The data merging occurs in several substeps, as illustrated in Figure 3.

[22] *Step 1.* Based on available but sparse grid matches (or match points) spatially complete global maps of ratios R between trusted reference data and background data are determined: Independently for continental and for oceanic regions, AERONET/modeling local data ratios at match points are spread over

Table 1. Annual Midvisible Aerosol Column Optical Properties of the MAC-v1 Climatology for Aerosol Optical Depth (AOD), Single Scattering Albedo (SSA), and Size-Related Asymmetry-Factor (ASY) and Equivalent Central Values From Aerosol Component Global Modeling (AeroCom) for Comparison^a

0.55 μm	AOD					SSA				ASY	
MAC-v1	Total	Coarse	Fine	Anthrop.	Natural	Total	Coarse	Fine	Anthrop.	Coarse	Fine
Global	0.130	0.069	0.061	0.037	0.093	0.958	0.982	0.932	0.927	0.76	0.57
Ocean	0.113	0.066	0.046	0.025	0.088	0.971	0.988	0.946	0.939	0.76	0.57
Land	0.178	0.076	0.101	0.070	0.107	0.938	0.969	0.916	0.916	0.77	0.56
AeroCom	Total	Coarse	Fine	Anthrop.	Total ^b	Total	Coarse	Fine	Total ^b	Coarse	Fine
Global	0.107	0.055	0.052	0.032	0.122	0.959	0.971	0.945	0.965	0.77	0.67
Ocean	0.091	0.051	0.040	0.026	0.104	0.972	0.985	0.953	0.977	0.76	0.68
Land	0.146	0.064	0.082	0.045	0.165	0.945	0.947	0.938	0.945	0.78	0.67

^aAnnual averages for totals and subcomponents for AOD, SSA, and ASY are presented for the entire globe, for ocean regions only, and for continental regions only for the MAC-v1 climatology and for the AeroCom median. The AeroCom median data are based on aerosol component median data, combining sulfate, and carbon to “fine” and combining dust and seasalt to “coarse.”

^bAverages for model-median maps of total AOD and of total SSA yield higher averages than the component-wise addition.

larger surrounding domains ($\pm 180^\circ$ longitude and $\pm 45^\circ$ latitude) with distance decaying weights $(1 + \text{dist}[\text{deg}])^{-1}$. Once data of all match points have been spread, locally at each grid point ratios are determined according to the associated weights. The combination of all local ratios globally establishes a global correction ratio map (for continents and oceans).

[23] *Step 2.* For each match point, an application domain is established. Within these domains weight fractions W are assigned. These grid weight fractions decay linearly from $W = 1.0$ at the originating grid to $W = 0.0$ at the domain boundary. The size of the spatial domain for a match point is tied to the highest range score of all contributing sites to that grid point. For land sites, the range-score associated domain (diameters of about 100, 300, 500, and 900 km for scores of 0, 1, 2, and 3) is doubled and quadrupled for ocean sites. Moreover, to account for an expected higher zonal similarity, the longitudinal domain is quadrupled, whereby a preferential stretch direction (via a cosine weight) was imposed according to prevailing winds: A maximum easterly stretch is assumed at midlatitudes (near 55°N or 55°S) and a maximum westerly stretch is assumed at the equator. In case of domain overlaps, the largest grid weight fraction is used.

[24] *Step 3.* Local correction factor F maps are determined: At each grid point the domain weight fraction W is multiplied with ratio R of the ratio map to establish the correction factor $F = W \times R + (1 - W) \times 1.0$ (where a ratio of 1.0 represents no change). These correction factors F are applied at each grid point to the background data. This completes the merging process.

[25] This merging process is applied to monthly maps of four midvisible (550 nm) aerosol column optical properties of AOD, SSA, AAOD, and AnP.

2.6. Results

[26] Global midvisible AOD maps are presented in Figures 1 and 2. Seasonal average AOD maps in Figure 1 demonstrate the strong seasonal variations associated with dust (e.g., over the Sahara and its outflow during northern hemisphere [NH] spring and NH summer) and

biomass burning (e.g., over West Africa in NH winter and NH fall over South America and southern Africa). In Figure 2, annual average maps for total midvisible AOD are paired with AOD maps displaying their contributions from aerosol with radii larger than $0.5 \mu\text{m}$ (coarse mode) and aerosol with radii smaller than $0.5 \mu\text{m}$ (fine mode). The procedure, that separates fine-mode and coarse-mode AOD contributions via AnP, is explained in section 3.1. The global distribution AOD patterns for coarse mode and fine mode are quite different even though their respective contribution to the annually and globally averaged midvisible AOD is similar. Hereby, higher coarse-mode AOD values are associated with dust (e.g., northern Africa) and sea salt (e.g., southern oceans), whereas higher fine-mode AOD contributions are registered over regions of urban pollution and regions affected by biomass burning. Also presented in Figure 2 is a map estimate for the annual anthropogenic AOD for the year 2000 with the help of global modeling. While the anthropogenic definition will be explained later, it is pointed out that the global annual midvisible anthropogenic AOD estimate (of 0.037) is only a small fraction of the global AOD (of 0.130). A comparison of the corresponding maps also shows that the anthropogenic AOD fraction near pollution centers is certainly higher.

[27] The merging process modified the background fields. New average values for aerosol column optical midvisible properties of AOD (corresponding to maps of Figure 2), SSA, and AnP are listed in Table 1. Averages are provided for global-only, ocean-only, and land-only data. Comparisons between the original annual maps for midvisible AOD, SSA, AAOD, and AnP and the same maps after the (merging) adjustment are presented in Figure 4. The adjustment changes to the background maps illustrate general deficiencies in global modeling. AOD, representing aerosol amount, is overall slightly increased by about 7% on a global average basis. Regional AOD increases are largest over South America and southern Africa (biomass burning fires), over southern and eastern Asia (pollution), and over Arabia (dust). In contrast, AOD is reduced over

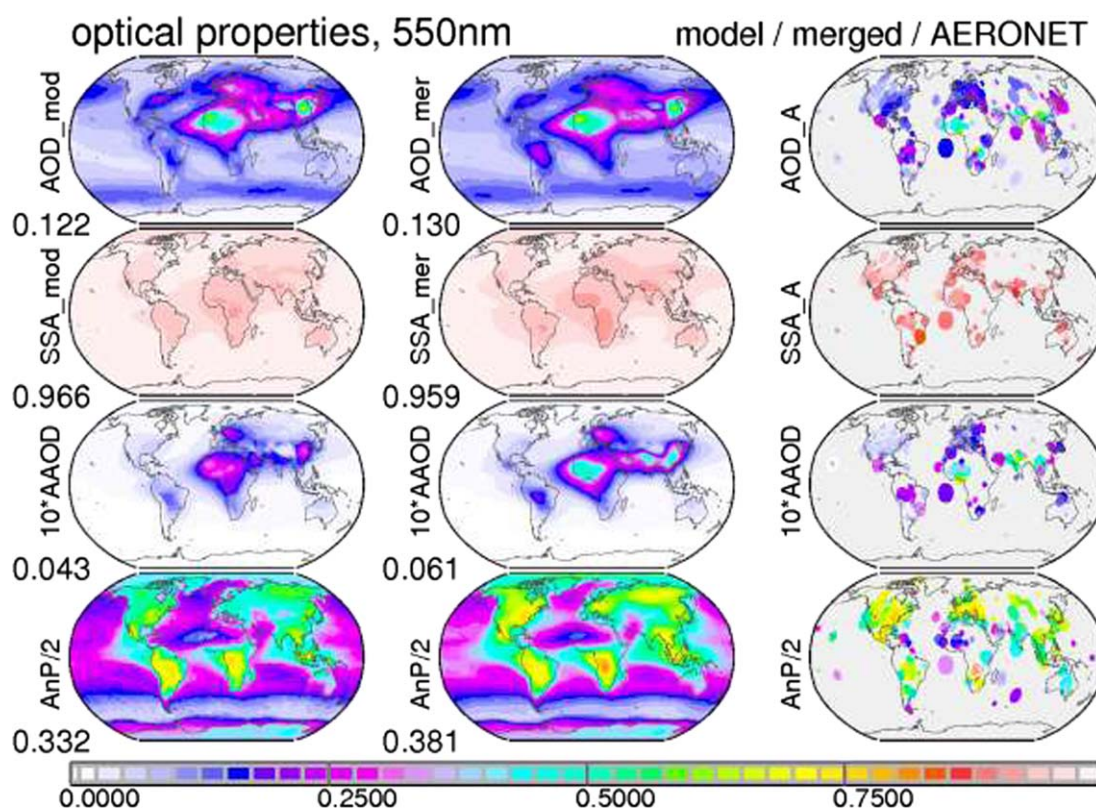


Figure 4. Global annual maps for tropospheric AOD, SSA, AAOD, and AnP (note AnP values are divided by 2 and AAOD are multiplied by 10 to fit the common scale). Compared are background (model ensemble median) maps (left column) before and (middle column) after the merging. (right column, enlarged for better viewing) Also presented are applied reference data of AERONET. Values below the labels are global (annual) averages. Note that at times (right column) larger SSA local AERONET data were not (or not in full) considered in the SSA adjustments because at low AOD data, the SSA retrievals are less reliable. Also, the (not used) AAOD adjustment resulted in stronger absorption than the SSA adjustment.

Europe and the eastern U.S. (pollution). SSA is now slightly reduced so that the absorption increases by about 25% (30% ocean, 22% land). For AAOD data (not used in MAC-v1, due to high bias concerns), the increases to absorption data are slightly larger at about 40% (48% ocean, 35% land). Regional absorption increases are largest over Africa and southern Asia. AnP, which indicates the relative importance of small aerosol sizes, is increased by about 15% (18% ocean, 8% land). Absolute increases to AnP are strongest over urban and biomass (tropical and boreal) regions.

[28] In summary, the merging of the AERONET data (on a global average basis) increases aerosol amount, increases aerosol absorption and reduces aerosol size of the background data (from global modeling). All three adjustments often occur together and are more significant during dry seasons over regions affected by biomass burning or by pollution. This is a hint that assumed aerosol emissions in modeling may need to be revisited (e.g., underestimates for tropical and boreal biomass emissions, underestimates for urban emissions over SE Asia, but overestimates for urban emissions over Europe). Some efforts are underway to address emission errors with inverse modeling methods [e.g., *Schutgens et al.*, 2012].

2.7. Comparisons

[29] To understand strengths and limitations of this new MAC-v1 climatology, comparisons are conducted to complementary available data set, including data from satellite remote sensing. Four alternate AOD data sets are introduced by their global annual maps in Figure 5. These are midvisible AOD data of (1) the AeroCom model median (which served as background in the merging process), (2) of the sparsely distributed AERONET network, (3) of the Tanre-climatology (which served as standard default in older ECHAM climate model versions), and (4) of a satellite remote sensing composite. The satellite composite involves independent AOD retrievals with MODIS, MISR, and AVHRR sensor data. The composite picks on a regional basis the best performing multiannual retrieval with respect to AERONET statistics in terms of bias, spatial correlation, and temporal correlation and combines the selected regional choices to global maps [Kinne, 2009]. Annual regional AOD biases of the new MAC-v1 climatology with respect to these four data sets (of Figure 5) are presented in Figure 6.

[30] There are surprisingly large AOD differences between satellite composite and the new MAC-v1 climatology. The MAC-v1 climatology shows larger AOD

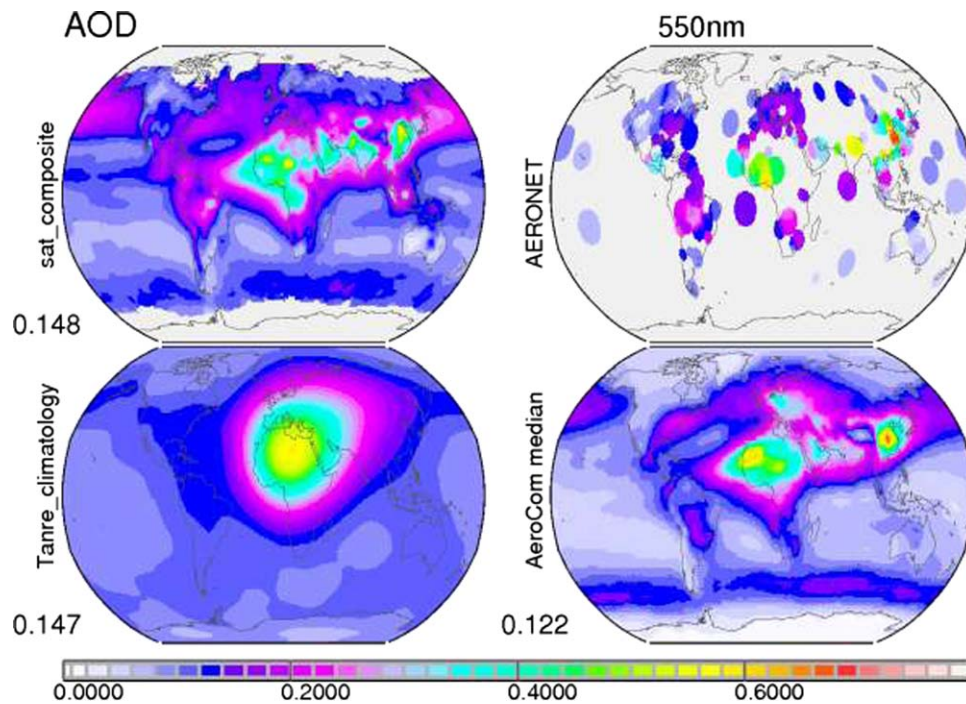


Figure 5. Annual average maps of alternate data sources for the tropospheric midvisible AOD. A best estimate of remote sensing from (top left) a combination of different satellite retrievals, (bottom left) the dated Tanre climatology, (top right) AERONET ground data, and (bottom right) a global model median. Values below the labels indicate global averages.

values over Eastern Europe, central eastern Asia, and the western Sahara, but lower AOD values over tropical Africa and Indonesia. The larger AOD values over

Europe are in part a merging technique issue, since AERONET data in that region are consistently lower: Due to a too wide longitudinal spread for the ratio map

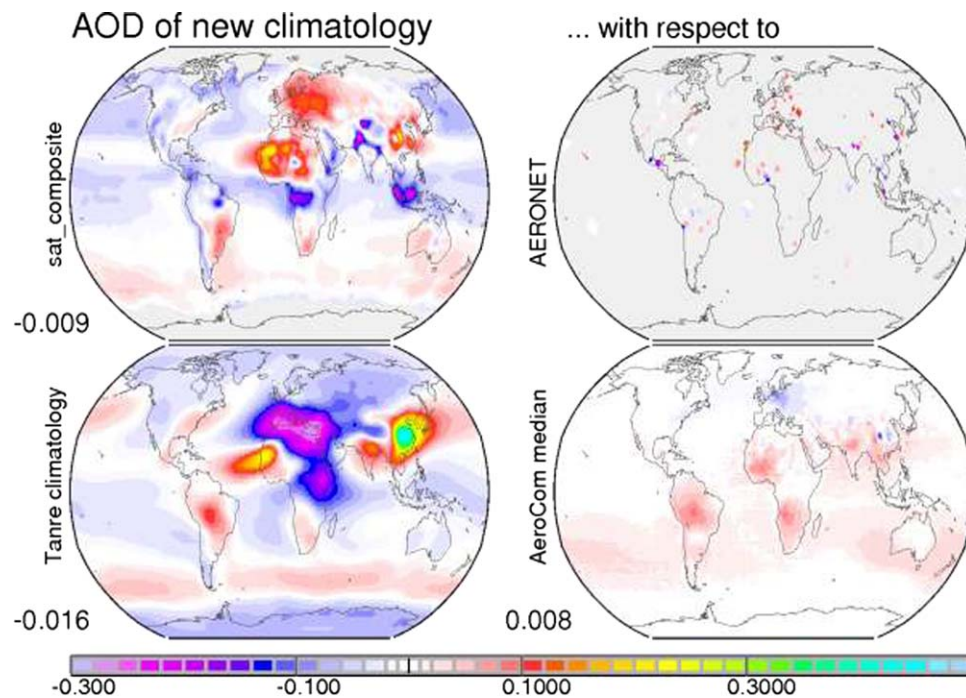


Figure 6. AOD annual biases of the new climatology (see Figure 2, top left) with respect to other data sets (presented in Figure 5). Values below the labels indicate global averages.

AOD reductions are regionally too weak. The larger AOD values over eastern Asia and northern Africa may in part be related to a satellite retrieval sampling issue. Both regions are influenced by dust. And strong dust events are often removed in cloud screening procedures prior to the aerosol retrieval. The lower AOD values over central Africa and Indonesia may be related to a priori biases in satellite retrievals, as strong absorption by wildfire aerosol when extended beyond biomass burning regions or seasons results in AOD retrieval overestimates. Lower AOD values over northern India are likely a climatology bias, as emission input for the model defining background is too weak and AERONET sites, needed for the adjustment, are too sparse.

[31] Temporal trends are a contributing element in explaining AOD differences between the MAC-v1 climatology (model year 2000 AERONET, 1996–2008) and the satellite composite (2000–2010). Most differences are such that major regional AOD trends identified by satellite remote sensing are not fully included. Satellite-based AOD trends between 2000 and 2010 [e.g., *Hsu et al.*, 2012; *Stevens and Schwartz*, 2012] indicate AOD increases over the Arabic Peninsula and southern Asia, but AOD decrease over the western Sahara and the associated outflow region over the Atlantic. Also small AOD decreases are observed for Europe and the U.S. Since, AERONET and applied global modeling generally refers to a time periods in the early 2000s, compared to the late 2000s of satellite data, some of the AOD differences between satellite composite and MAC-v1 climatology can be attributed to a temporal mismatch. Additional comparisons between AOD values of the new MAC-v1 climatology and global multiannual AOD data of satellite retrievals by MODIS [*Levy et al.*, 2010] and by CALIPSO [*Winker et al.*, 2007] are found elsewhere [*Pappas et al.*, 2013].

[32] Also shown in Figure 6 are differences with respect to the older Tanre climatology, which was developed in the mid-1980s. Then aerosol loads were stronger over Europe and weaker over eastern and southern Asia and very little was known about the seasonal biomass burning contributions of the Southern Hemisphere. The displayed differences to the Tanre climatology mainly indicate AOD deficiencies of the older and now outdated climatology, including overestimates over Europe and over the Sahara, but underestimates over eastern Asia, over biomass regions of the Southern Hemisphere and over the Southern Oceans.

[33] A more general approach is a comparison of global averages. Global, oceanic, and continental global annual averages for midvisible aerosol column properties of AOD, SSA, and ASY of the MAC-v1 climatology are summarized in Table 1. (ASY represents the asymmetry-factor, which is an inverse measure for aerosol size.). Particularly interesting are comparisons to averages by similar merging methods, which also involve monthly statistics of AERONET. A method that fits empirical orthogonal function of (MODIS) satellite data and (GOCART) modeling data to AERONET data for a 2 year period [*Liu et al.*, 2005] yields a global annual midvisible AOD of 0.130, identical to that of the MAC-v1 climatology. Similarly, another

merging method that also combines (MODIS) satellite AOD data and (GOCART) model output with AERONET data [*Chung et al.*, 2005] yields a similar global annual AOD (0.127). Their ocean averages are slightly smaller (0.104 compared to 0.113), while their continental averages are slightly larger (0.183–0.178). Differences are larger for the aerosol absorption. Their associated SSA values are significantly lower. As these lower values rely on the BC-type fraction by one (GOCART) model, which is known for relatively high BC-ratios compared to those of other global models [*Kinne et al.*, 2006], it is plausible that their global SSA of 0.942 is biased low. The SSA value of the MAC-v1 climatology of 0.958, as listed in Table 1, is based on an SSA merging. Note that a slightly lower SSA of 0.953 is determined when absorption would have been defined via AAOD merging instead.

[34] Aside from averages of the MAC-v1 climatology also corresponding averages of the AeroCom phase 1 model median are listed in Table 1. Since the model median maps defined the background, differences to the MAC-v1 average indicate elements of adjustments due to the merging process. The model median AOD is slightly smaller (AOD: 0.122 versus 0.130) but significantly smaller (AOD: 0.107 versus 0.130) when adding the five components of the model median. The AOD partition into coarse-mode and fine-mode contributions is quite similar with an overall slightly larger coarse-mode AOD fraction (~52%), a larger coarse-mode fraction over oceans (~57%), and a smaller coarse-mode fraction over continents (~43%). The absorption potential (1-SSA) is smaller for the model median, especially for fine-mode aerosol over continents (SSA: 0.938 versus 0.916). Also the fine-mode particles of the model median are larger as illustrated by the smaller asymmetry-factor for the fine mode (ASY: 0.57 versus 0.67). Thus, the merging of the sun-photometer data (1) slightly raises the background AOD, (2) strongly increases background absorption by fine-mode aerosol, and (3) reduces the fine-mode aerosol size.

3. Spectral Expansion

[35] The spectral extension of midvisible aerosol column optical properties to other wavelengths of the solar spectrum and to wavelengths of the (far-) infrared spectrum (from now referred to as subspectral properties) is simplified with the assumption that tropospheric aerosol size distributions are bimodal. Aerosol size is usually characterized by two distinct size modes that are optically active. Particle formation processes including gas to particle conversion (e.g., sulfate, nitrate, secondary organics) are main contributors to the fine-mode aerosol sizes covering the radius range between 0.05 and 0.5 μm . And primary emitted sea salt (evaporation of sea spray) and lifted soil-dust are the main contributors to the coarse-mode aerosol sizes covering the radius range between 0.5 and 15 μm .

3.1. Midvisible AOD Partitioning

[36] The separation of the AOD into contributions by fine-mode aerosol (AOD_F) and contributions by

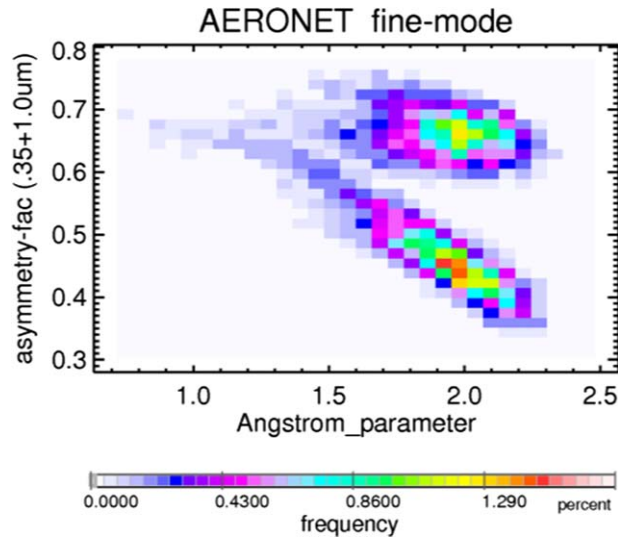


Figure 7. Probability distribution of between the fine-mode Angstrom parameter and the asymmetry factors of fine mode aerosol at (top cluster) 0.35 μm and (bottom cluster) 1.0 μm .

coarse-mode aerosol (AOD_C) is done with the help of the midvisible Angstrom parameter (AnP) of the new MAC-v1 climatology. To do this, of course, the Angstrom values of the coarse-mode and fine-mode must be known. Coarse-mode particles are large enough to not display any significant spectral AOD dependence in the solar spectrum. So the Angstrom parameter of the coarse mode is assumed to be zero ($\text{AnP}_C = 0$), which approximately applies to all assumed coarse mode size distributions. Fine-mode particles have smaller AOD values at larger solar wavelength, so much so that the Angstrom parameter of the fine mode is greater than 1 and can even exceed 2 ($1 < \text{AnP}_F < 2.5$). Usually it can be stated, that the smaller the characteristic size, the larger AnP_F . A distribution on AERONET statistics for the fine-mode Angstrom parameters in Figure 7 indicate that typical AnP_F values vary between 1.6 and 2.2. It is now assumed that the main reason for this diversity is aerosol size swelling by water uptake although aerosol aging and cloud processing also contribute: An AnP_F value of 2.2 refers to dry (or fresh) conditions, while an AnP_F value of 1.6 refers to water saturated (or aged) conditions: $\text{AnP}_F = 2.2 - \log[1 + 0.6 \times C_{\text{LOW},s}]$, where $C_{\text{LOW},s}$ is the scaled low-level cloud cover ($C_{\text{LOW},s} = C_{\text{LOW}}/[1 - C_{\text{MID}} - C_{\text{HIGH}}]$) of the ISCCP multianual monthly cloud climatology [Rossow *et al.*, 1993], which is chosen to substitute for ambient relative humidity. At this point $\text{AnP}_C (=0)$ and AnP_F are defined so that with the overall Angstrom parameter of the MAC-v1 climatology (AnP) the total AOD can be split into fine-mode AOD (AOD_F) and coarse mode AOD (AOD_C). In extreme cases, AOD is completely assigned to either AOD_C or AOD_F only, if AnP falls outside the range provided by AnP_F and AnP_C . The separation for the annual AOD is presented in Figure 2.

3.2. Coarse-Mode Aerosol Type and Size Selection

[37] The local midvisible SSA value of the MAC-v1 climatology is used to define the coarse-mode composition. Coarse aerosols are assumed to be sea salt, dust, or a combination of both. In the midvisible solar region, sea salt is nonabsorbing ($\text{SSA}_{\text{SS}} = 1.0$) and dust is absorbing ($\text{SSA}_{\text{DU}} < 1.0$). Hereby the actual SSA_{DU} value depends on the assumed dust size, with lower SSA_{DU} associated with larger dust sizes. Thus, the SSA MAC-v1 value of the climatology can and actually is also used to retrieve information on dust aerosol size.

[38] Based on the SSA of the climatology, an initial guess for the coarse-mode SSA (SSA_C) is derived by assuming that the fine mode is 10 times more absorbing than the coarse mode. Assuming initially a relative small coarse dust size ($r_{\text{eff}} = 1.5 \mu\text{m}$), the midvisible SSA value for coarse dust is defined ($\text{SSA}_{\text{DU}} = 0.967$). Recalling the nonabsorbing nature of sea salt ($\text{SSA}_{\text{SS}} = 1.0$), locally an initial dust fraction (DU_f) is derived from SSA_C . With the assumption that at larger AOD_C a dust presence becomes more likely, the initial DU_f is linearly increased for $\text{AOD}_C > 0.1$ to the point that at $\text{AOD}_C > 0.3$ the entire coarse mode is dust. With a DU_f increase the SSA_C is automatically lowered, but only to the point that this new SSA_C cannot fall below the SSA value of the new climatology.

[39] Now the focus turns to the fine-mode SSA (SSA_F). SSA_F can be determined, because values are given for AOD_C , AOD , SSA_C , and SSA . To avoid unrealistically low SSA_F data, a minimum $\text{SSA}_{F_{\text{low}}}$ value is defined such that the SSA_F cannot fall below 0.75 unless AOD values are very small ($\text{SSA}_{F_{\text{low}}} = 1 - 0.25 \times \text{AOD}_F - 0.1 \times \exp[-3 \times \text{AOD}]$). If the determined SSA_F value falls below this $\text{SSA}_{F_{\text{low}}}$ threshold then SSA_F is set to $\text{SSA}_{F_{\text{low}}}$ and the extra SSA reduction is compensated by an increase in dust size (e.g., r_{eff} of 2.5 or 4.0 μm have lower midvisible SSA_{DU} values of 0.949 and 0.926). Resulting dust size increases occur (as expected) mainly over the Sahara desert regions. At this stage the midvisible SSA_F is determined, the composition of the coarse mode is established and the dust size is defined.

3.3. Coarse-Mode Aerosol Optical Properties

[40] The radiative properties of the coarse mode are defined by two components. These are either sea salt ($r_{\text{eff}} = 2.0 \mu\text{m}$) and dust of a relatively small initial size ($r_{\text{eff}} = 1.5 \mu\text{m}$) or these are two different dust sizes, based on five different predefined dust size choices ($r_{\text{eff}} = 1.5, 2.5, 4.0, 6.5, 10 \mu\text{m}$). Assuming log-normal size-distributions, all needed spectrally dependent radiative properties (AOD, SSA, and ASY) for the one sea salt and the five dust sizes were precalculated via MIE simulation [Dave, 1968]. The needed refractive indices for sea salt [Nilsson *et al.*, 1979] and dust (I. Sokolik, 2005, personal communication) are listed in Table 2. The spherical shape assumption of MIE simulations is not optimal for (nonspherical) dust, but resulting errors with respect to radiative fluxes are minor. One of the needed properties (aside AOD and SSA) is the asymmetry-factor (ASY). ASY summarizes, as cosine weighted integral, the behavior of directional scattering (e.g., the closer to 1.0, the stronger the forward scatter).

Table 2. Refractive Indices (Real and Imaginary Part) for Dust and Sea Salt at Central Wavelengths of (Left) Solar and (Right) Infrared Subspectral Bands of ECHAM6

Solar					Infrared				
λ (μm)	Dust		Sea Salt		λ (μm)	Dust		Sea Salt	
	RI, real	RI, imag	RI, real	RI, imag		RI, real	RI, imag	RI, real	RI, imag
0.23	1.53	0.20–1	1.51	0.10–4	3.60	1.46	0.11–1	1.48	0.16–2
0.30	1.53	0.10–1	1.51	0.10–5	4.00	1.49	0.47–2	1.48	0.18–2
0.40	1.53	0.50–2	1.50	0.20–7	4.20	1.49	0.53–2	1.49	0.25–2
0.55	1.53	0.18–2	1.49	0.10–7	4.60	1.50	0.84–2	1.48	0.25–2
0.70	1.53	0.70–3	1.48	0.10–6	5.20	1.60	0.22–1	1.46	0.29–2
1.00	1.52	0.70–3	1.47	0.10–3	6.15	1.42	0.51–1	1.51	0.18–1
1.27	1.52	0.80–3	1.47	0.33–3	7.00	1.44	0.10	1.45	0.54–2
1.46	1.51	0.12–2	1.46	0.55–3	7.85	1.23	0.84–1	1.40	0.14–1
1.78	1.51	0.25–2	1.45	0.10–2	8.85	1.55	0.44	1.64	0.29–1
2.05	1.50	0.50–2	1.45	0.15–2	9.75	2.96	0.89	1.56	0.18–1
2.32	1.50	0.10–1	1.44	0.25–2	11.2	1.81	0.28	1.49	0.14–1
2.79	1.49	0.35–1	1.40	0.80–2	13.2	1.71	0.21	1.41	0.19–1
3.47	1.46	0.12–1	1.48	0.13–1	15.1	1.51	0.22	1.45	0.34–1
8.00	1.17	0.10	1.40	0.14–1	18.0	1.93	0.52	1.76	0.11
					30.0	2.42	0.68	1.75	0.25
					100.0	2.40	0.70	1.62	1.00

[41] The radiative properties of the two component mixtures (sea salt and dust or two different dust sizes) are then combined according to the mixing rules: AOD is additive, SSA is AOD-weighted, and ASY is (AOD \times SSA)-weighted. All spectrally resolved coarse-mode optical properties are now defined: AOD_C, SSA_C, and ASY_C.

3.4. Fine-Mode Aerosol Optical Properties

[42] Spectrally resolved fine-mode optical properties (AOD_F, SSA_F, and ASY_F) are only required for the solar spectrum, as particles are too small for significant interactions with infrared radiative transfer. Some properties were already defined, such as midvisible properties for AOD_F, AnP_F, and SSA_F. At other solar wavelengths λ the fine-mode AOD is defined using AnP_F: AOD(λ) = exp {−AnP_F \times ln (λ [μm]/0.55) + ln(AOD_F)}. For the spectral dependency of the fine-mode SSA, the midvisible SSA_F (which was determined when assigning the coarse-mode composition) is extended over the entire visible and UV solar spectrum ($\lambda < 0.7 \mu\text{m}$). For longer solar wavelengths (into the near-infrared spectrum), the fine-mode SSA is increasingly reduced, because in the Rayleigh regime (when particle size is significantly smaller than the wavelength) the scattering drops faster (λ^{-4}) than the absorption (λ^{-1}) with increasing wavelength. Finally, the asymmetry factor of the fine mode (ASY_F) is based on an AERONET-based relationship for the fine-mode Angstrom parameter of the new climatology (AnP_F): ASY_F(λ) = max {0.72 − 0.14 \times AnP_F \times (λ [μm] − 0.2)^{0.5}, 0.1}. This simple parameterization, which estimate the solar asymmetry-factor of fine-mode aerosol as function of the fine-mode Angstrom parameter AnP_F and the solar wavelength λ is tied to AERONET based joint probability distributions of monthly statistics between AnP_F and ASY_F at different solar wavelengths, as illustrated in Figure 7 for ASY_F at 0.35–1.0 μm .

3.5. Results

[43] Annual average coarse-mode and fine-mode optical properties of AOD, SSA, AAOD (=AOD \times [1 − SSA]), and ASY are compared to the combined (total) aerosol optical properties at a midvisible wavelength in Figure 8. The associated annual global, oceanic and continental averages for AOD and SSA are listed in Table 1. As already mentioned in the discussions to Figure 2, there are striking differences to the AOD patterns, despite similar global annual average contributions to the midvisible AOD by the fine mode (AOD_F of about 0.61) and by the coarse mode (AOD_C of about 0.69). Absorption is illustrated by the relative potential via the 1-SSA and by the absolute measure of the AAOD. In the MAC-v1 climatology, the fine-mode absorption potential (SSA_F of about 0.93) is much stronger than the coarse-mode absorption potential (SSA_C of about 0.98). Also the absorption potential is stronger over land (SSA_{LAND} of about 0.94) than over oceans (SSA_{OCEAN} of about 0.97). In terms of absolute absorption patterns, the coarse mode reaches only over the Sahara an absorption strength that is comparable to fine-mode absorption maxima over industrial and biomass burning regions. Finally, coarse-mode particles have a stronger forward scatter and are even less absorbing in the midvisible, so that ASY values of the coarse mode have to be larger (ASY_C of about 0.76) than those of the fine mode (ASY_F of about 0.57).

[44] The previous aerosol column optical properties referred to the midvisible spectral region. In addition, based on the previously explained spectral extension, global maps for aerosol optical properties of AOD, SSA, and ASY at selected other wavelengths are presented in Figure 9. For the demonstration maps at three wavelengths have been selected, one in the UV (400 nm), one in near-infrared (1 μm), and one in the far-infrared (10 μm). The associated annual global, oceanic

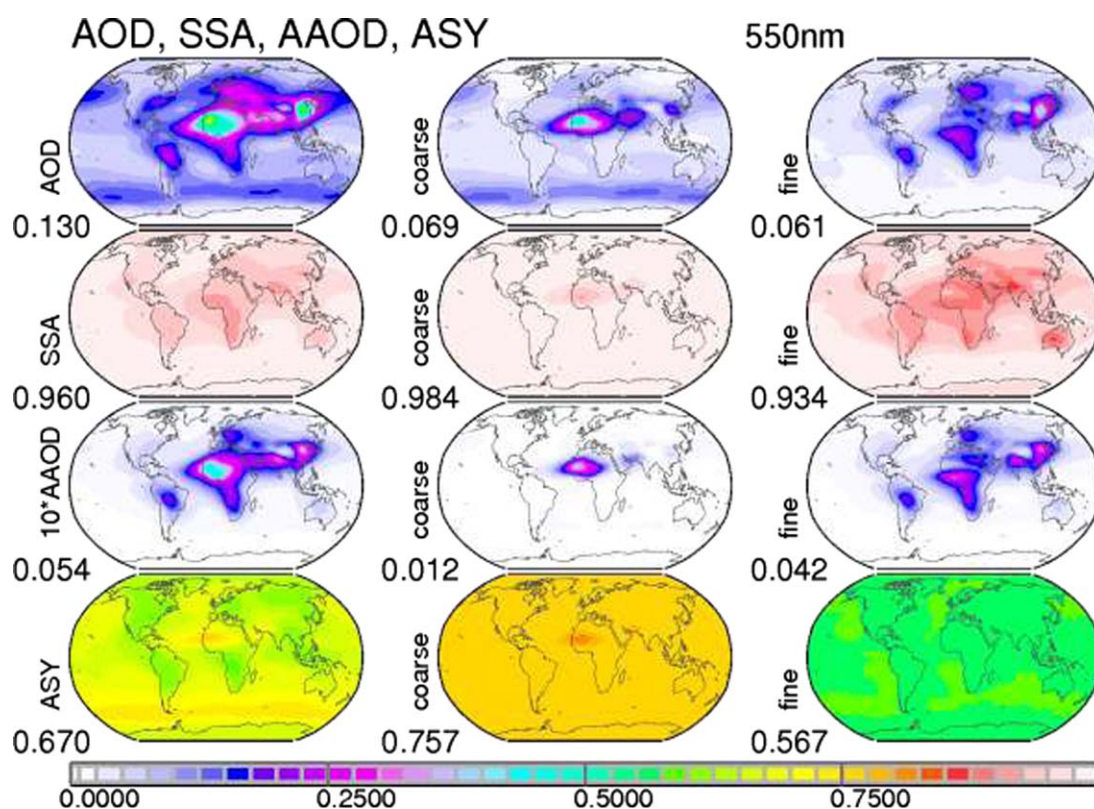


Figure 8. Annual average maps for the tropospheric midvisible aerosol optical properties of the new aerosol climatology. AOD, SSA, AAOD (times 10), and ASY are presented for (left column) total aerosol as well as those (middle column) by coarse-mode aerosol only, and (right column) by fine mode aerosol only. Values below the labels indicate global averages.

and continental averages are listed in Table 3. The fine mode dominates the aerosol properties in the UV but has reduced contributions in the near-IR and no contributions in the far-IR. The coarse-mode properties in the far-IR differ significantly from the midvisible coarse-mode properties (compare to Figure 8), as refractive indices and the ratio between aerosol size and applied wavelength are different.

4. Vertical Distribution

[45] The aerosol altitude distribution is an important element when addressing aerosol climate impacts. Passive remote sensing, however, offers (little to) no information on aerosol altitude. Thus, data from simulations with a complex aerosol module are applied. More specifically, simulations with year 2000 emissions [Dentener et al., 2006] were performed with the ECHAM5-HAM model [Stier et al., 2005]. Global monthly 3-D distributions for midvisible AOD are used to define fractional AOD contribution for 20 preselected altitude layers (with layer boundaries at 0.0, 0.5, 1.0, 1.5, 2.0, 2.5, 3.0, 3.5, 4.0, 4.5, 5, 6, 7, 8, 9, 10, 11, 12, 13, 15, and 20 km above the sea level). These fractional contributions are multiplied with the midvisible AOD of the new climatology to define the vertical distribution of aerosol. This altitude assignment is done separately for optical depths of the fine-mode (AOD_F),

the coarse-mode (AOD_C), and the combined total AOD. AOD assignments for four preselected altitude regimes of 0–1, 1–3, 3–6, and 6–12 km are compared in Figure 10. In terms of global annual averages, coarse-mode contributions are stronger below 1 km, while fine-mode contributions are larger above 3 km.

[46] An alternate data set to describe the aerosol vertical distribution could have been the CALIPSO lidar [Winker et al., 2007], although it would have been difficult to provide the needed separation between coarse and fine mode. In addition, at the time of data preparation only older CALIPSO version 2 data were available, which had known deficiencies. A recent comparison of aerosol vertical distributions of different global models with newer CALIPSO version 3 data [Koffi et al., 2012] indicates that many global models place aerosol on average at too high altitudes. On the other hand, in this comparison ECHAM5-HAM with its relative low-aerosol placement among available global models, is one of few models that compares rather well to CALIPSO statistics. Thus, the use of ECHAM5-HAM seems preferable over the use of a model ensemble to describe the aerosol vertical distribution.

[47] In the MAC-v1 climatology, coarse-mode and fine-mode aerosols radiative properties are independently determined and so is their AOD altitude distribution. Any altitude dependence for the other radiative parameters, SSA and ASY, which prescribe the aerosol

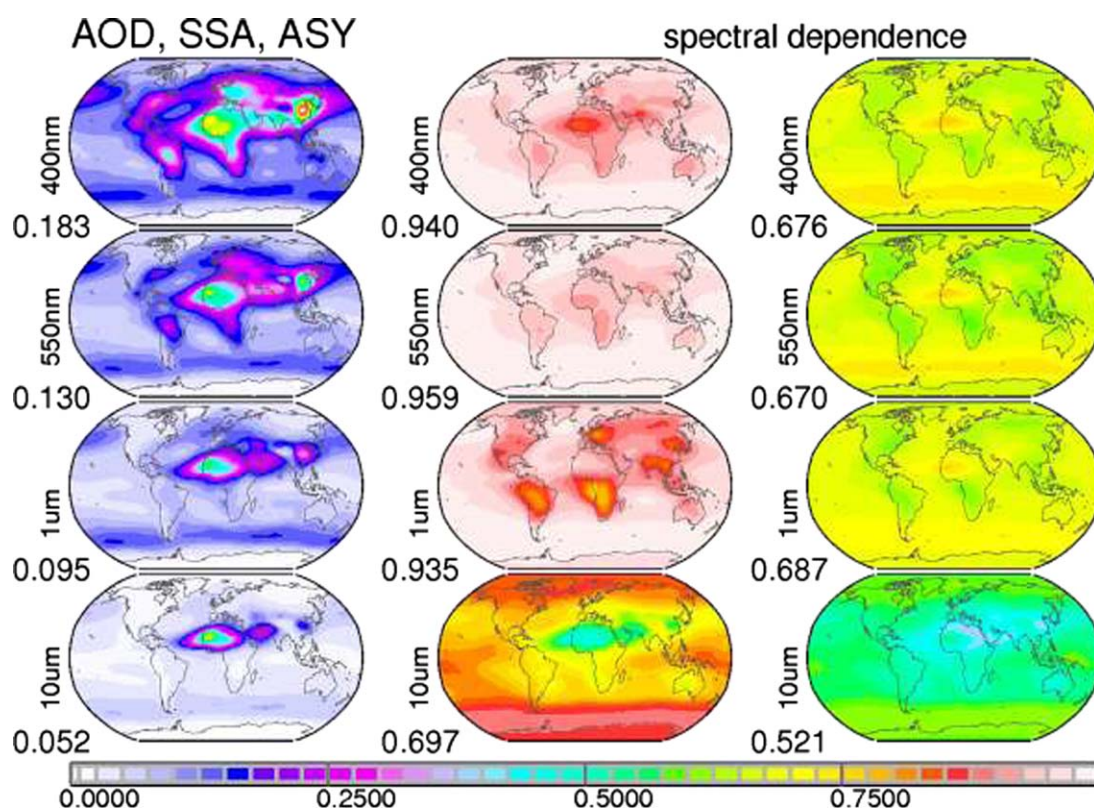


Figure 9. Spectral dependencies for the tropospheric (left column) AOD, (middle column) SSA, and (right column) ASY of the new climatology. Data are presented for a wavelength in the UV (400 nm, row 1), midvisible (0.55 μm , row 2), the near-infrared (1 μm , row 3), and in the far-infrared (10 μm , row 4). Values below the wavelength labels indicate global averages.

composition, are ignored. SSA and ASY for total aerosol, however, will vary with altitude, as soon as the ratio between fine-mode AOD and coarse-mode AOD are changed. Such changes occur when a part of the temporal expansion the anthropogenic (fine mode) AOD is modified, which is explained next.

5. Temporal Variations

[48] Aside from seasonal variations also decadal changes are prescribed. Interannual changes are

permitted only to anthropogenic AOD, thus no changes to natural aerosol other than its seasonal cycle are allowed. This approach required a separation of the AOD in natural and anthropogenic contributions. First, the anthropogenic AOD maps for current (year 2000) conditions are established before these maps are scaled back and forward in time.

5.1. Anthropogenic AOD of the Year 2000

[49] For climate studies, aerosol anthropogenic contributions are often more interesting than total

Table 3. Spectral Dependence of Annual Aerosol Column Optical Properties of the MAC-v1 Climatology for Aerosol Optical Depth (AOD), Single Scattering Albedo (SSA), and Asymmetry Factor (ASY) at Selected Wavelengths in the UV, Near-IR, and Far-IR (Complementing Midvisible 0.55 μm Averages of Table 1) for Total and for Anthropogenic Aerosol^a

	AOD			SSA			ASY		
	0.4 μm	1 μm	10 μm	0.4 μm	1 μm	10 μm	0.4 μm	1 μm	10 μm
Total									
Global	0.183	0.095	0.052	0.938	0.936	0.681	0.676	0.690	0.521
Ocean	0.150	0.088	0.046	0.954	0.955	0.737	0.686	0.694	0.537
Land	0.265	0.112	0.067	0.916	0.898	0.586	0.662	0.680	0.485
Anthr									
Global	0.070	0.011	0.003	0.927	0.692	0.312	0.567	0.479	0.378
Ocean	0.045	0.008	0.002	0.939	0.733	0.362	0.570	0.484	0.385
Land	0.132	0.020	0.006	0.916	0.656	0.266	0.563	0.473	0.368

^aAverages are presented for the entire globe, ocean only, and land only (top part) for total and (bottom part) for anthropogenic aerosol properties.

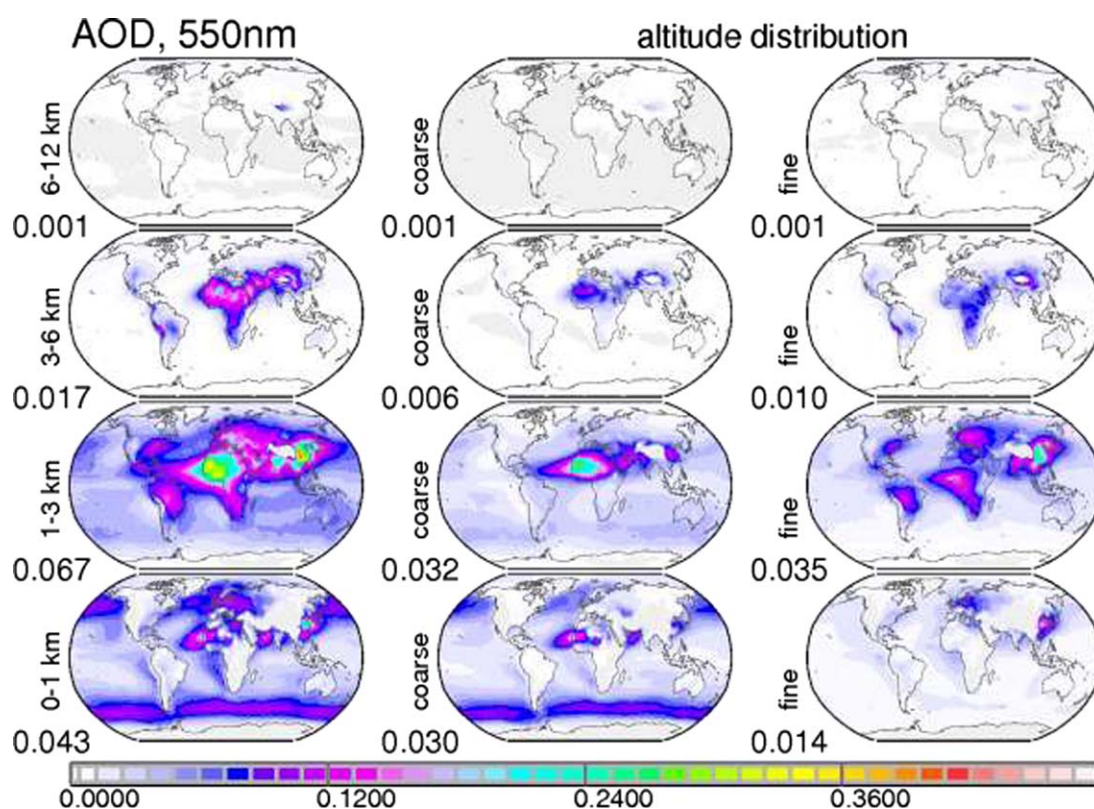


Figure 10. Vertical distribution of the current (year 2000) midvisible AOD for (left column) total aerosol, (middle column) coarse mode aerosol, and (right column) fine-mode aerosol based on the relative altitude distribution of ECHAM5-HAM simulations. AOD values are presented for four different altitude regime above sea levels. Values below the labels indicate assigned global annual AOD averages for current (year 2000) for each altitude regime.

(including natural) contributions although natural contributions alone are usually stronger. The desired separation into anthropogenic and natural contributions, however, requires knowledge about aerosol properties at preindustrial times. Preindustrial conditions can at best be estimated but not measured. Thus, for the MAC-v1 climatology help from global modeling is needed to separate AOD into its anthropogenic and natural contributions.

[50] It is assumed that anthropogenic aerosol only contributes via fine-mode aerosol sizes. Thus, the entire coarse mode is considered natural in origin. To estimate the anthropogenic AOD fraction of the fine-mode aerosol at current (year 2000) conditions as it has ramped up from preindustrial times, results of two model simulations with the LMD model [Reddy and Boucher, 2004] are used. Applying recommended aerosol emissions [Dentener et al., 2006] as input, one simulation applies year 2000 emissions while the other simulation applies year 1750 emissions. Only monthly AOD_F maps of the two simulations are examined. The AOD_F increase between year 2000 and 1750 in reference to the year 2000 AOD_F defines $Fant_{2000}$ ($= [AOD_{F,2000} - AOD_{F,1750}] / AOD_{F,2000}$), the year 2000 anthropogenic AOD fraction of the fine mode.

[51] There are certainly uncertainties to the anthropogenic $Fant_{2000}$, mainly due to assumptions

when extrapolating emission back in time (in Dentener et al. [2006]) and due to the reliance on an appropriate aerosol processing in the LMD aerosol component module. There also could be a low bias, because anthropogenic dust (e.g., due to land-cover change) is ignored. On the other hand, linking anthropogenic to only the fine mode (instead of to the total AOD) avoids contaminations by interannual variation of the (mainly natural) coarse mode, which at least on a global average basis, as mentioned above, has much larger AOD contributions.

[52] Seasonal maps of $Fant_{2000}$ are presented in Figure 11. The global distribution displays a strong hemispheric asymmetry. Higher fractions on the order of 90% are found over industrial regions of the Northern Hemisphere, whereas fractions over the Southern Hemisphere are much smaller and only on the order of 10% over southern hemispheric oceans. Multiplying this fraction with the AOD_F maps of the climatology yields anthropogenic AOD for the year 2000 (as illustrated by the annual average in Figure 2). The other optical properties characterizing the composition of anthropogenic aerosol (SSA and ASY) are assumed identical to that of the fine-mode aerosol (and the fine-mode aerosol at preindustrial times).

[53] The assumed global annual average for the current anthropogenic midvisible aerosol optical depth (of 0.037) is rather central to a relative wide range of

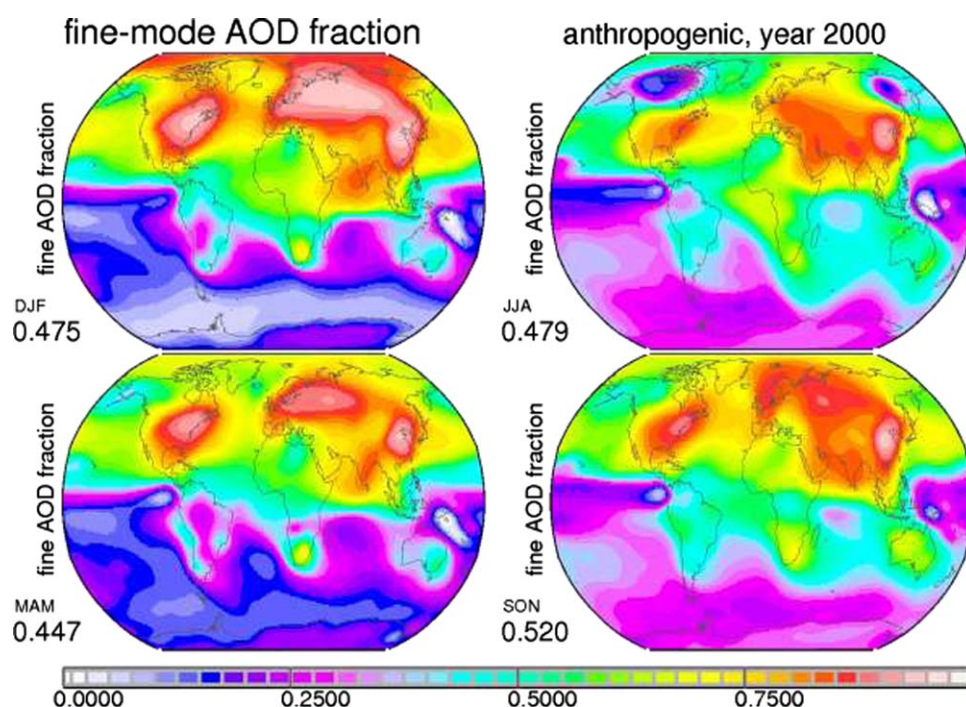


Figure 11. Seasonal maps for the fraction of current (year 2000) fine-mode AOD attributed to anthropogenic sources. Values below the labels indicate global seasonal averages.

0.030–0.050 in global modeling [Schulz *et al.*, 2006]. In the context of subsequent comparisons for aerosol radiative effects, it is also noted that in a similar merging study [Chung *et al.*, 2005] relatively large anthropogenic midvisible aerosol optical depth (of 0.051) is applied along with a much stronger aerosol absorption (SSA of 0.868 instead of 0.932 in MAC-v1). These very low SSA values are difficult to explain in the context of available AERONET observations and their 2.5 times larger anthropogenic aerosol absorption over the MAC-v1 climatology remains highly questionable.

[54] All nonanthropogenic aerosol particles are considered natural by default. Thus, natural aerosol includes aside from all coarse-mode particles also fine-mode particles that already existed at preindustrial times. In terms of the midvisible AOD for current (year 2000) conditions natural contributions of about 0.093, with 0.069 from coarse mode and 0.024 from the (preindustrial) fine mode, clearly dominate anthropogenic contributions of about 0.037.

5.2. The Industrial Era

[55] The definition of historic aerosol properties from current (year 2000) conditions back in time to preindustrial (1850) conditions involves a few basic assumptions. The only quantity allowed to vary with time is the anthropogenic aerosol optical depth, which is a fraction of the fine mode. This means that the remaining (preindustrial) fine-mode and coarse-mode aerosol with their year 2000 monthly varying optical properties remain constant in time. Also the monthly varying relative altitude profiles for coarse-mode and fine-mode AOD of current (year 2000) conditions are applied for all other years.

[56] Central to the definition of historic aerosol properties are continuous ECHAM5-HAM model [Stier *et al.*, 2005] simulations (at T63, L19 resolution) from 1850 to 2010 with emission input data provided by the National Institute for Environmental Studies in Japan (NIES). Surface temperature and sea ice concentrations were simulated by the Earth-System model. The HAM aerosol module processes aerosol by type and provide output for seven-size classes (three insoluble and four soluble). With the focus on smaller (fine mode) aerosol, only the two (insoluble and soluble) classes of the accumulation size mode (radii between 0.05 and 0.5 μm) are of interest. Even smaller size classes of the nucleation and Aitken mode are ignored, because they are not optically active.

[57] The overall concept is to capture the regional and seasonal change of the fine-mode AOD (AOD_F) over time. The ECHAM5-HAM simulations are used to increase, starting from the preindustrial AOD_F baseline, locally the anthropogenic fine-mode AOD fraction $\text{Fant}_{1850} = 0.0$ at preindustrial times to $\text{Fant}_{2000} = 1.0$ at current (year 2000) conditions. In order to reduce interannual noise, data are summarized into decadal multiannual averages and smoothing (via regional interquartile averages) is applied. Smoothed fine-mode AOD data for the 1850–1860 time period define the preindustrial background. Then based on smoothed AOD_F data local scaling factors are calculated for each decade. These scaling factors were not allowed to be negative but certainly could be larger than 1.0. Larger values are common for Europe in the later part of the 20th century, when anthropogenic (fine mode) AOD was

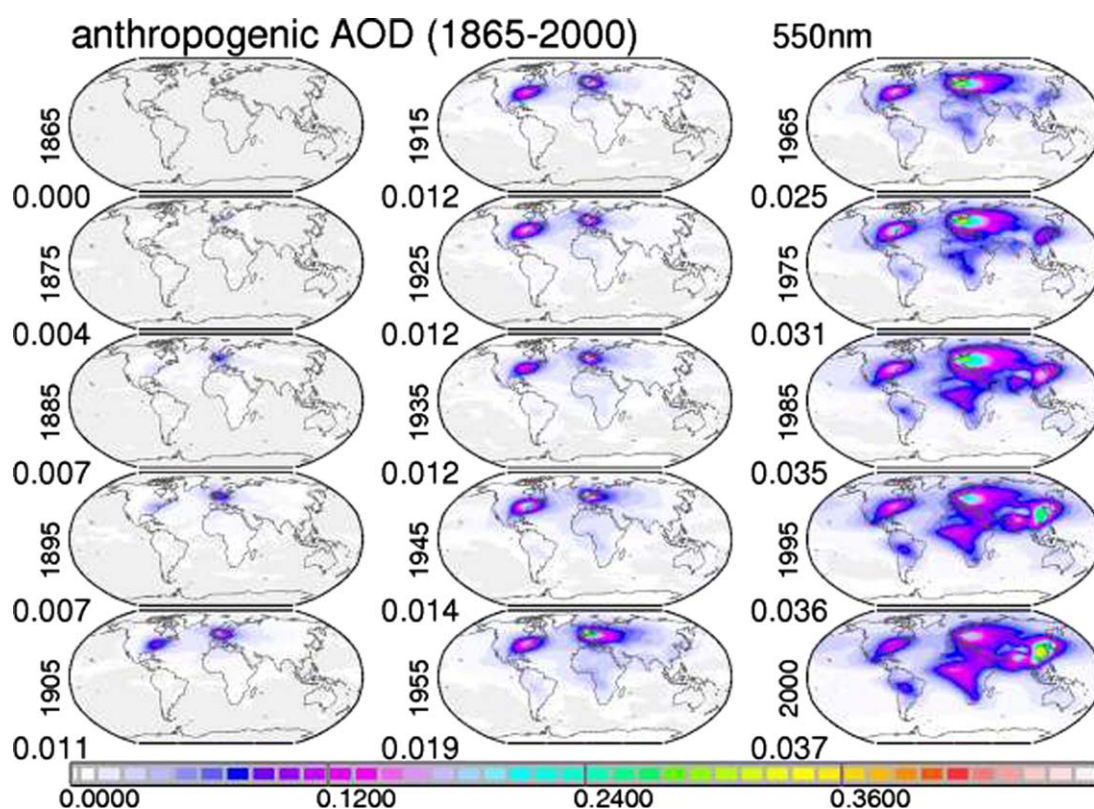


Figure 12. Annual average maps of historic midvisible anthropogenic aerosol optical depth for selected years. The values below the labels indicate global annual averages.

stronger than nowadays. Decadal scaling factors are assigned the central year of each decade (e.g., 1865, 1985) and scaling factors of in-between years resulted from linear interpolation.

[58] ECHAM5-HAM based historic scaling factors are applied to the previously defined anthropogenic AOD at current (year 2000) conditions of the new aerosol climatology. The resulting AOD maps are presented in Figure 12. Note the strengthening over bipolar distributions with maxima over Europe and the U.S. well into the second half of the 20th century. Only during the last decades of the 20th century increasing contributions are added from other continental regions, most prominently from eastern and southern Asia and western Africa, while contributions from Europe and the U.S. after reaching maxima in the 1970s have been declining.

5.3. Future Scenarios

[59] The definition of future aerosol properties from current (year 2000) conditions forward in time until the year 2100 involved the same basic assumptions as for historic aerosol properties. The only quantity allowed to vary with time is the anthropogenic aerosol optical depth, which is a fraction of the fine mode. This means that the remaining (preindustrial) fine-mode and coarse-mode aerosol with their year 2000 monthly varying optical properties remain the same for each year. Also the monthly varying relative altitude profiles for

coarse-mode and fine-mode AOD of reference (year 2000) conditions are applied for all other years.

[60] Central to the definition of future aerosol properties are three different RCP (2.6, 4.5, and 8.5) emission scenarios [Moss *et al.*, 2010] for sulfate and organics, which were developed (by independent groups) in support of the IPCC fifth assessment. Rather than relating AOD_F directly to emissions, simulations with the HAM aerosol component module within the framework of the ECHAM5 global model were performed to account for aerosol transport and aerosol processing.

[61] To explore impacts on AOD_F from changes in regional emissions, the globe was subdivided into 10 major emission regions (which are defined in IPCC RCP scenario data). In 10 different simulations, sulfur emissions in each region were reduced by 50% (with respect to year 2000 conditions) and then global distributions of AOD_F were compared to those of the reference year 2000. Carbonaceous emission reductions were also considered but in the end not applied, because sensitivity studies revealed less significant impacts on AOD_F compared to sulfur reductions. Simulations apply ECHAM5-HAM (at T42, L19 resolution) with prescribed climatological sea surface temperature and sea ice concentrations. Output results with reduced sulfur emissions by region were averaged over 10 year periods. The quantity of interest is the regional change to the fine-mode aerosol optical depth (AOD_F) compared to a scenario using the full sulfur emissions. Hereby,

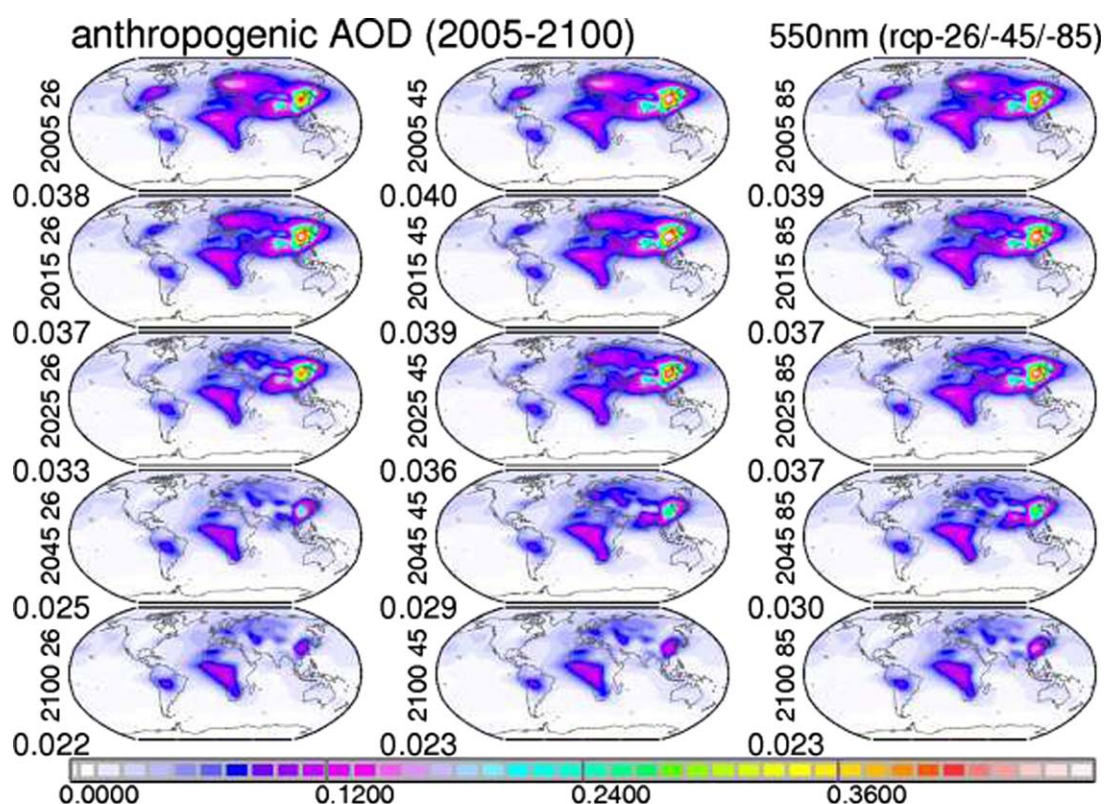


Figure 13. Annual average maps of midvisible anthropogenic aerosol optical depth for selected future years of three different IPCC emission scenarios (left column) rcp2.6, (middle column) rcp4.5, and (right column) rcp8.5. Values below the labels indicate global averages.

changes (usually reductions) to AOD_F also occur over neighboring regions, where sulfur emissions had remained in full. Knowing the global AOD_F response to regional emission reductions, three different future sulfur aerosol emission scenarios are applied, as prescribed by the RCP-2.6, RCP-4.5, and RCP-8.5 scenarios of the IPCC fifth assessment [Meinshausen *et al.*, 2011; Lamarque *et al.*, 2010]. Hereby, the AOD_F response is derived by linearly relating the actual sulfate emission changes to those of the 50% reduction in the test simulations. An AOD_F response is only considered, if the perturbation was significant (based on a student t test with 10×12 samples). At each grid box changes in AOD_F due to sulfate changes in all 10 regions are summed for the overall change in local AOD_F . This overall local AOD_F change is added to the AOD_F of year 2000 conditions. In order to avoid a negative anthropogenic AOD, the only prescribed boundary condition is that local reductions for AOD_F cannot drop below the preindustrial AOD_F value. (Thus, in unexpected cases of very strong sulfur reductions so that estimated future AOD_F (locally) drops below the preindustrial AOD_F value, this boundary conditions could cause a slight overestimate for the derived future anthropogenic AOD.)

[62] Based on the ratio of emission related AOD_F changes to the anthropogenic AOD of the model at current (year 2000) conditions, local scaling factors are defined for each decade and assigned to the central year

of its decade. Scaling factors of in-between years resulted from linear interpolation. Finally, these scaling factors are applied to the anthropogenic AOD of the new aerosol climatology at current (year 2000) conditions and global maps for anthropogenic AOD in future years are determined. For selected future years, these anthropogenic AOD maps for the three emission scenarios are similar, as illustrated in Figure 13.

[63] The anthropogenic AOD maximum over eastern Asia is predicted to reach the largest values in the 2010s or 2020s, depending on the RCP scenario, and then rapidly declines. In most other regions, the anthropogenic AOD is expected to decline toward the future. Based on these estimates, the globally average anthropogenic AOD may have already reached its maximum and significant reductions are expected toward the year 2100.

6. Radiative Effects

[64] An easy application of the new climatology is the determination of direct aerosol radiative effects. A simple radiative transfer code is applied twice with and without aerosol so that differences to calculated solar and infrared radiative fluxes define the aerosol direct radiative impacts. Appendix A briefly summarizes the applied computational environment.

[65] Dual radiative transfer simulations with and without aerosol are performed for clear-sky (no clouds) and all-sky conditions. From differences in solar

Table 4. Simulated Global Annual Averages for Aerosol Direct Effects (in W/m^2)

Global (W/m^2)	Solar and Infrared		Solar (only)		Anthropogenic	
	Clear-Sky	All-Sky	Clear-Sky	All-Sky	Clear-Sky	All-Sky
Top of atmosphere	−3.4	−1.6	−4.5	−2.1	−1.0	−0.5
Atmosphere	2.8	3.1	3.7	3.6	1.5	1.4
Surface	−6.2	−4.7	−8.2	−5.7	−2.5	−1.9
Ocean (W/m^2)	Clear-Sky	All-Sky	Clear-Sky	All-Sky	Clear-Sky	All-Sky
Top of atmosphere	−4.1	−2.1	−5.0	−2.5	−0.9	−0.5
Atmosphere	1.5	1.8	2.3	2.2	0.8	0.8
Surface	−5.6	−3.9	−7.3	−4.7	−1.7	−1.3
Land (W/m^2)	Clear-Sky	All-Sky	Clear-Sky	All-Sky	Clear-Sky	All-Sky
Top of atmosphere	−1.6	−0.2	−3.1	−1.2	−1.2	−0.4
Atmosphere	6.3	6.5	7.4	7.2	3.3	3.2
Surface	−7.9	−6.7	−10.5	−8.4	−4.5	−3.6

(broadband) and infrared (broadband) fluxes, aerosol direct effects are derived for total and anthropogenic aerosol. Interesting in particular are aerosol radiative effects on net fluxes at the top of the atmosphere (TOA) and at the surface, as well as their differences. TOA impacts address the climate impact to the Earth-Atmosphere-System and TOA data also can be directly related to satellite observations. Surface impacts influence surface processes and near surface conditions. And local differences between TOA and surface net fluxes differences address atmospheric heating or cooling, with their potential impacts on atmospheric dynamics and the hydrological cycle.

[66] Global, oceanic and continental annual averages for aerosol direct radiative effects at current (year 2000) conditions are listed in Table 4. Relationships among the average in the tables illustrate that

[67] 1. Solar aerosol direct radiative effects dominate IR aerosol direct radiative effects.

[68] 2. Infrared aerosol direct radiative effects are nonnegligible (as natural coarse-mode aerosol on averages offsets about 25% of the solar aerosol direct radiative effects).

[69] 3. Anthropogenic aerosol direct radiative effects are much smaller than total aerosol direct radiative effects.

[70] 4. Aerosol direct radiative effects at TOA are less negative than at the surface—due to atmospheric direct radiative effects.

[71] 5. Atmospheric direct radiative effects over continents are 3–4 times stronger than over oceans.

[72] 6. Atmospheric direct radiative effects (mainly solar warming) for clear-sky conditions are similar to the atmospheric direct radiative effects for all-sky conditions.

[73] 7. Aerosol direct radiative effects at TOA and aerosol direct radiative effects at the surface are larger for clear-sky conditions compared to all-sky conditions. (At TOA, the gap between clear-sky and all-sky aerosol radiative effects is widened due to the dimming of cloud reflection by elevated absorbing aerosol.)

[74] The regional and seasonal distributions of aerosol direct effects are highly diverse and are explored

next. For current (year 2000) conditions, distribution maps associated with the annual global averages of Table 4 are presented in Figures 14–16.

6.1. Global Distributions

[75] Spatial distributions for annual average aerosol direct effects at TOA and surface, for all-sky and clear-sky conditions and for total (shortwave and longwave), solar (only shortwave), and anthropogenic impacts are compared in Figure 14. Direct radiative effects linked to anthropogenic aerosol are much smaller than those for total aerosol. Spatial distributions for all-sky (with clouds) and clear-sky (or cloud-free) conditions are similar, only weaker for all-sky conditions. At the TOA, aerosol solar cooling (indicated by negative values) occurs almost everywhere, except over regions with higher solar surface reflectance, including regions with significant snow cover (as for central Asian winter and spring) or with desert surfaces (as for northern Africa and Arabia). The aerosol solar warming (indicated by positive values) over many dust source regions is further warmed by the infrared greenhouse effect of elevated dust. For other regions, a considerable smaller infrared greenhouse effect can only slightly reduces the solar cooling. At the surface negative values, thus reduced radiative effects, are found everywhere in the annual average maps. Solar net-flux losses display a maximum over Northern Africa and at clear-sky conditions a secondary maximum over eastern Asia. When including infrared impacts (for total net-flux changes), however, the northern Africa maximum has disappeared, as solar losses are compensated by coarse mode generated infrared reradiation to the ground. Over the Sahara this reradiation by dust almost compensates solar losses, while only smaller solar loss reductions occur over oceanic midlatitude regions due to sea salt.

[76] Differences between TOA and surface radiative effects determine the atmospheric radiative effects or the divergence. Annual maps for current (year 2000) conditions are presented in the lower two rows of Figure 15. Hereby, a positive divergence represents atmospheric heating and a negative divergence stands

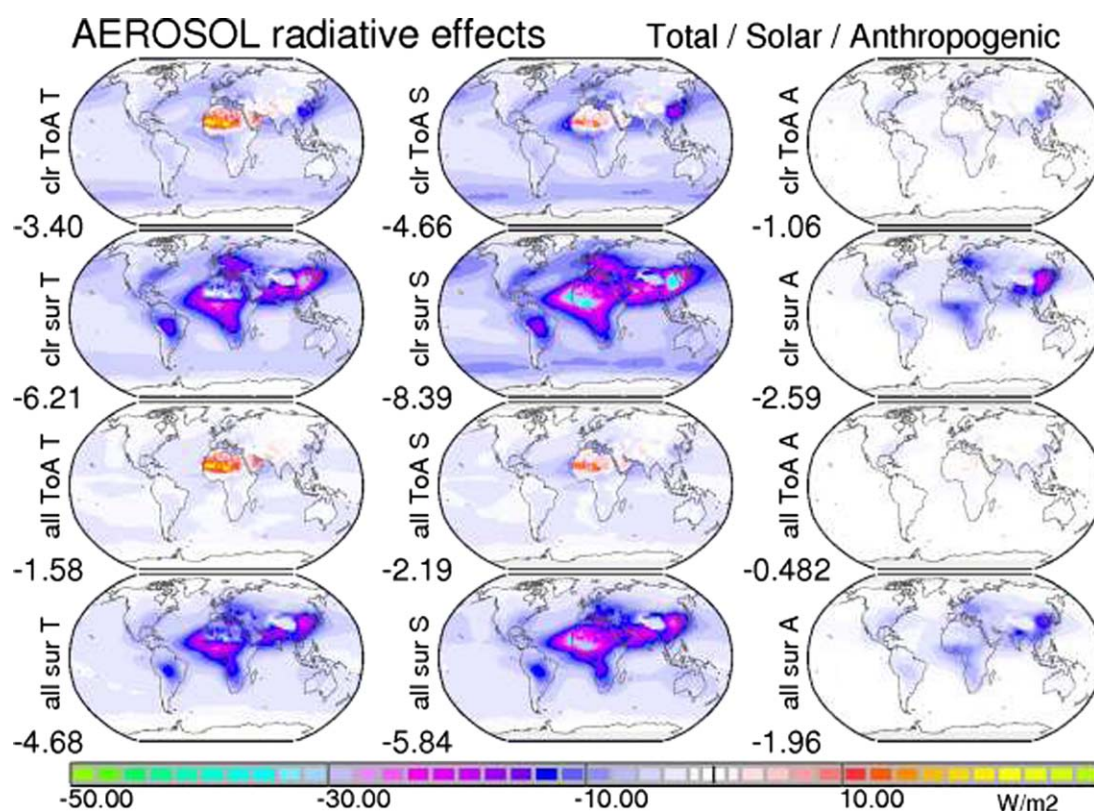


Figure 14. Annual average maps for aerosol direct radiative effects in W/m^2 . (left column) Combined solar and IR effects and (middle column) solar only effects for total aerosol are compared to radiative effects by (right column) anthropogenic aerosol. Annual maps are presented for clear-sky (cloud-free) conditions at (row 1) TOA and (row 2) surface and for all-sky conditions (with clouds) at (row 3) TOA and (row 4) surface. Values below the labels display annual global averages, which are also listed in Table 2.

for atmospheric cooling. The solar divergence is positive and largest in regions with strong aerosol absorption. To understand the divergence patterns, it should be recalled that the effective solar aerosol absorption involves not only the absorption potential (1-SSA) but also aerosol amount (AOD). Thus, even though dust has only a low-absorption potential, when combined with a large AOD value, the absorption by dust can be significant, as over northern Africa and Arabia. In contrast, BC has a high-absorption potential but usually negligible AOD—except over regions with strong pollution and strong biomass burning fires. Thus, stronger divergence values over eastern and southern Asia, southern America and southern and central Africa are mainly associated with BC. When including infrared impacts, the solar divergence is reduced over regions with atmospheric dust. Interestingly, the clear-sky and all-sky divergences are very similar.

[77] Differences between all-sky and clear-sky radiative effects determine the influence of colocated clouds on aerosol radiative effects. Annual maps of cloud effects on aerosol at current (year 2000) conditions are presented in the upper two rows of Figure 15. Clouds cause aerosol radiative effects to be less negative so that the (relative) impact of adding clouds is a warming. Reductions to the clear-sky aerosol radiative effects at

surface and TOA, however, is not symmetric, because aside from the cloud cover impact there is an added cloud altitude impact at TOA (when elevated absorbing aerosol dims the solar reflection of lower altitude clouds).

[78] Figure 16 redisplayes the anthropogenic aerosol radiative effects at TOA and at the surface for both clear-sky and all-sky conditions at a finer scale than in Figure 14. A comparison to the total aerosol radiative effects (in Figure 14) reveals similar spatial features but at reduced levels (when excluding the now missing maxima over dust regions). The reduction is caused foremost by the much lower AOD (see Table 1 or Figure 2) and at the TOA in addition by an increased relative absorption (compare SSA data in Table 1 or Figure 8). As a result, TOA radiative effects by anthropogenic aerosol turn positive over regions with brighter lower boundaries, such as over desert regions, over regions with snow and ice cover and over regions with lower altitude clouds (as for the Southeast Atlantic, where absorbing aerosol from biomass burning fires moves over lower stratus clouds).

6.2. Aerosol Forcing

[79] Direct aerosol forcing is (here) defined as the direct radiative effect at TOA under all-sky conditions

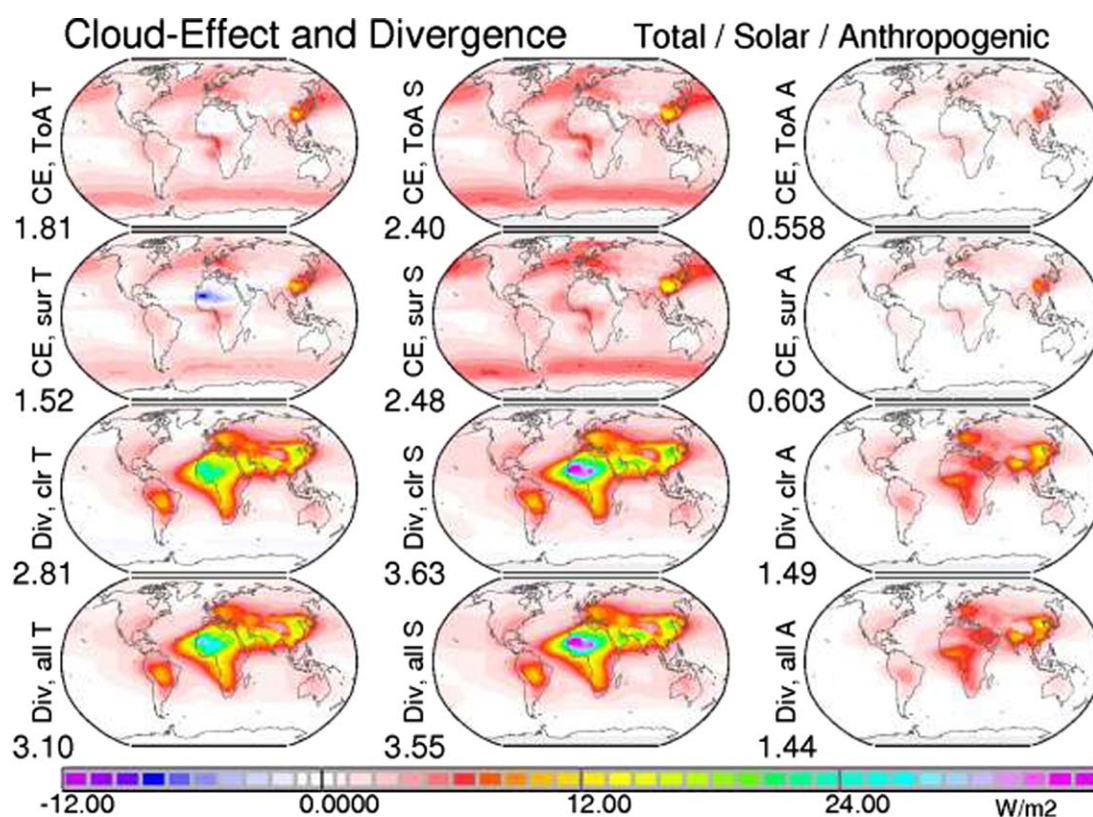


Figure 15. Annual average maps for the impact of clouds on aerosol radiative effects at (row 1) TOA and (row 2) surface and annual average maps for the aerosol associated atmospheric divergence (row 3) at clear-sky and (row 4) at all-sky conditions in W/m^2 . Compared are combined solar and (left column) infrared effects and (center column) solar only effects for total aerosol with effects for (right column) anthropogenic aerosol. Values below the labels display annual global averages, which are also listed in Table 2.

for anthropogenic aerosol. Direct aerosol forcing is the relevant aerosol forcing property in climate change considerations. While the annual aerosol forcing map for current (year 2000) conditions was already presented in Figure 16, the associated seasonal variations are presented in Figure 17. The direct aerosol forcing displays both positive and negative values. Hereby, positive values indicate warming and negative values indicate cooling. The sign of the seasonal aerosol direct forcing in many regions is quite sensitive to the seasonal variations of solar reflectance at lower altitudes. These variations are mainly caused by changes in snow cover or by changes to the presence of clouds below the aerosol altitude. Negative values throughout the year are displayed for most oceanic regions and for regions affected near urban industrial pollution centers, where climatic cooling by aerosol is strongest during the summer months. Regions with positive values throughout the year are found over desert regions of northeast Africa and Arabia. Regional and seasonal averages span the range from almost $\pm 5 \text{ W/m}^2$. This spatial and temporal variability is frequently ignored, when summarizing the aerosol climate impact by the single values of the global annual average (here -0.48 W/m^2).

[80] Temporal changes of the direct aerosol forcing from preindustrial times into the future (applying the

AOD maps of Figures 12 and 13) are presented in Figures 18–20. As can be noted in these plots, the forcing simulations were performed at lower spatial resolution (at 12×6 rather than at $1 \times 1^\circ$ longitude/latitude). Although lower resolution simulations reduce local maxima, they do not significantly influence global annual averages.

[81] Figure 18 illustrates the spatial build-up of the direct aerosol forcing from preindustrial times, which is almost entirely limited to Europe and to the U.S. Figure 19 presents changes in the direct aerosol forcing over the last 30 years with the shift of the maxima over Europe and the U.S. to eastern and southern Asia. Figure 20 finally presents the anticipated future decrease of the aerosol direct forcing based on IPCC future emission scenarios. The global mean aerosol forcing increase was strongest between 1965 and 1985 at about -0.08 W/m^2 per decade. Since 1980 the global averages aerosol direct forcing increases have slowed. The global aerosol direct forcing is projected to reach its maximum between 2010 and 2025. By 2100, all three scenarios indicate a direct anthropogenic aerosol forcing that on a global average basis is reduced back to levels of the year 1970. However, all future estimates are highly optimistic and may have a low bias, since future

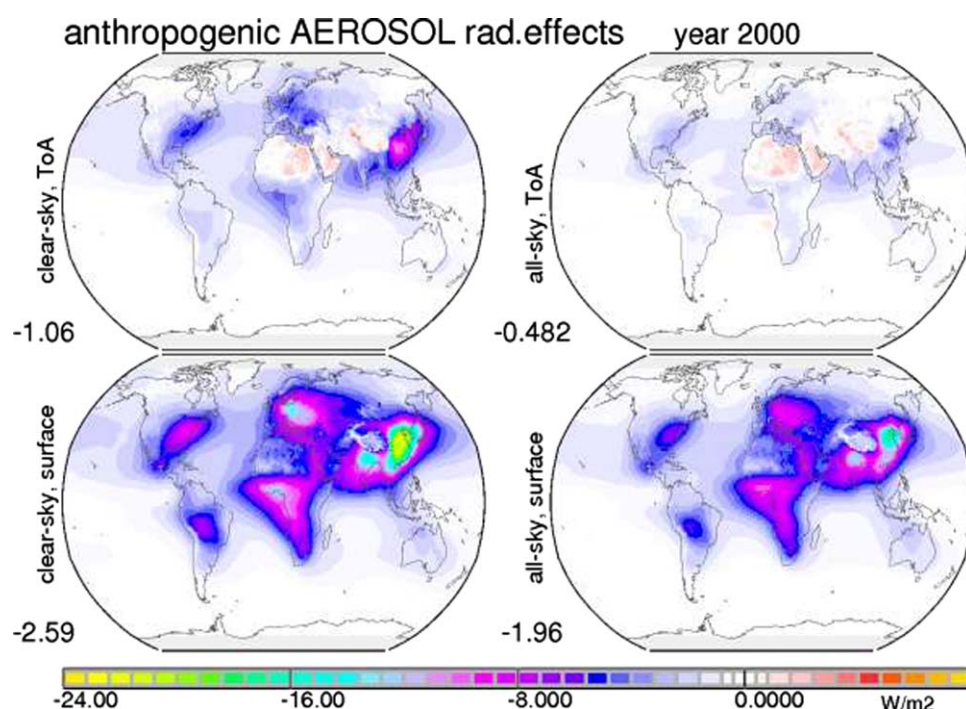


Figure 16. Annual maps for anthropogenic direct aerosol effects at (left column) clear-sky and (right column) all-sky conditions at (top row) TOA and (bottom row) surface in W/m^2 . (Note, all maps are identical to right column data of Figure 14, now at an expanded scale).

atmospheric anthropogenic aerosol loads were based on changes to anthropogenic sulfate. While sulfate indeed is expected to decrease in the future, other pollutants may remain at the same levels or even

increase, such as organics or nitrates [Bauer *et al.*, 2007; Bellouin *et al.*, 2011]. Despite similarities in the overall cooling by anthropogenic aerosol for the years 1970 and 2100, there are also significant

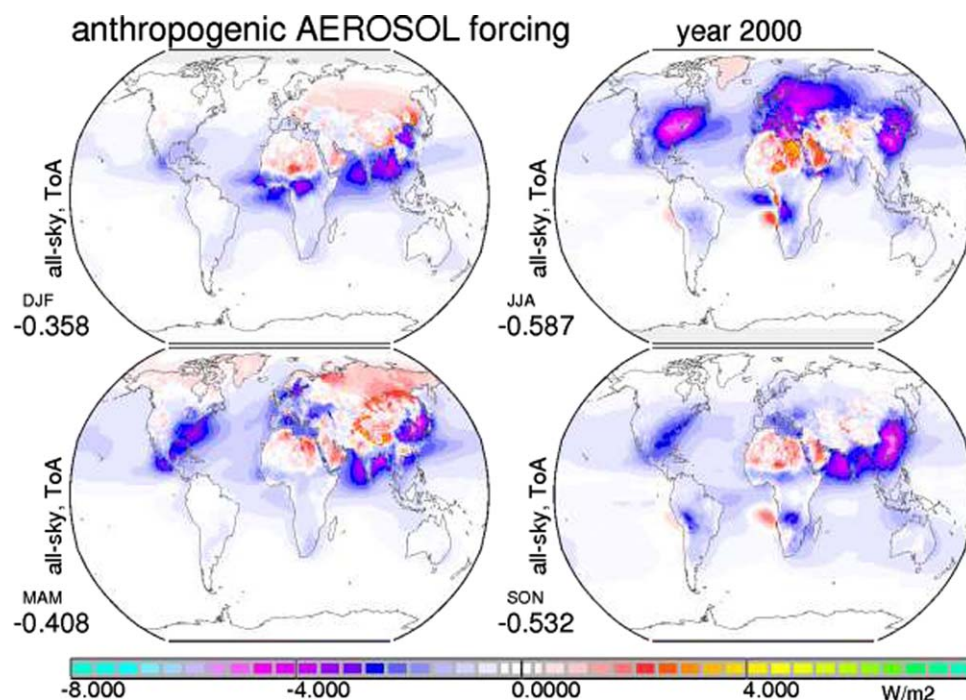


Figure 17. Seasonal maps for the current (year 2000) anthropogenic direct aerosol forcing (= aerosol direct radiative effects under all-sky conditions at TOA) in W/m^2 . Values below the labels display seasonal global averages.

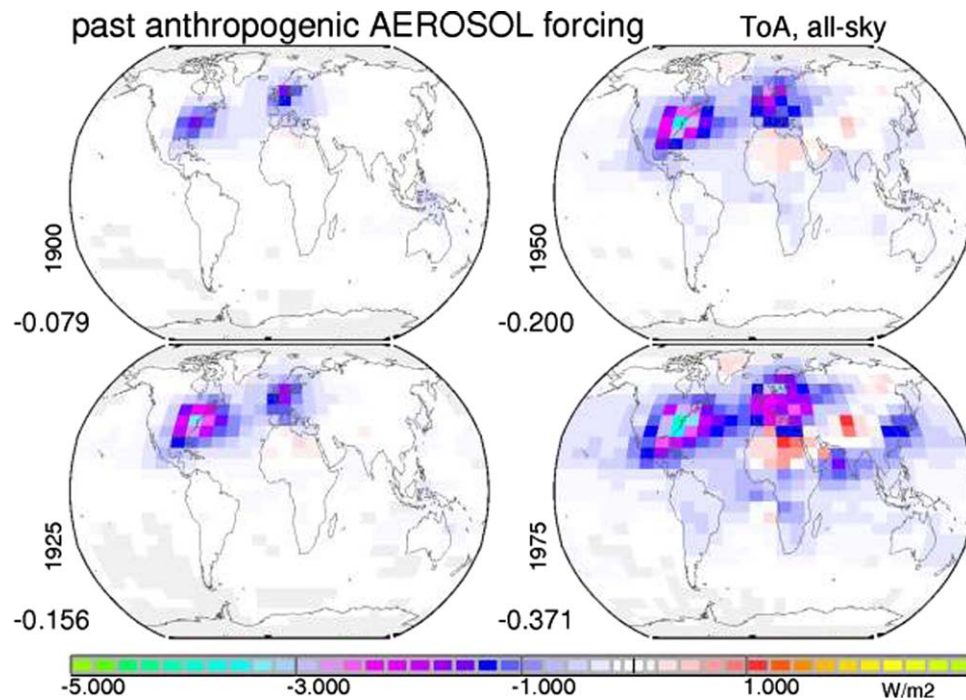


Figure 18. Annual average maps for historic time slices (years 1900–1975) for the direct anthropogenic aerosol forcing (all-sky, at TOA) in W/m^2 . Associated global averages are listed below labels.

regional differences that should be mentioned. There is a shift in maximum cooling from over the U.S. (1970) and Europe (1980) during the later decades of the last century, via unprecedented maxima over

southern and eastern Asia now (2020) and in the near future, to eventually weak maxima over central Africa and eastern Asia by the end for the century (2100).

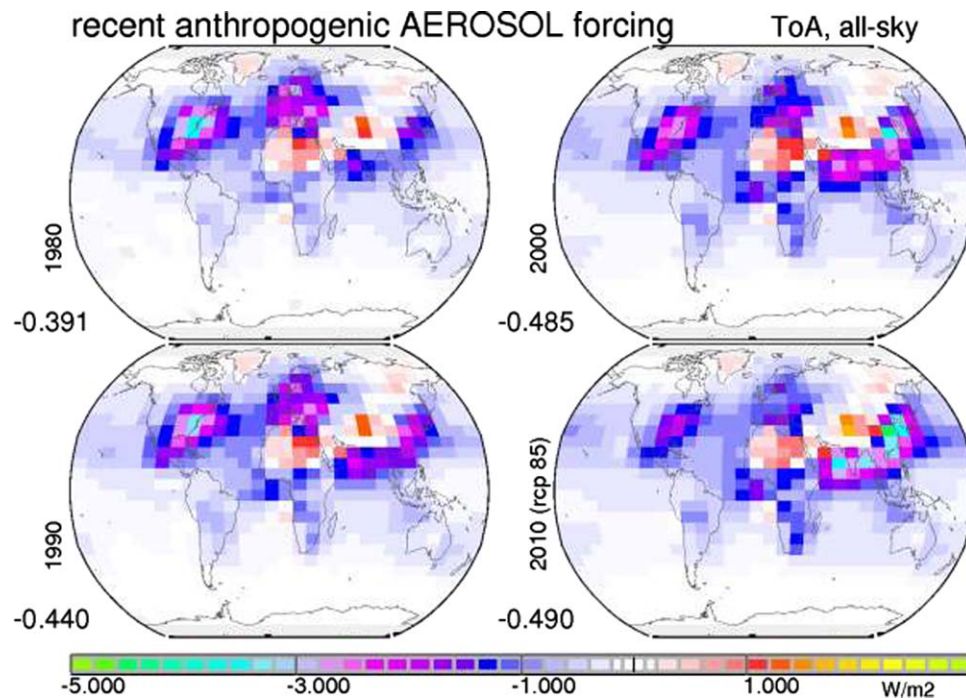


Figure 19. Annual average maps for more recent times slices (years 1980–2010) for the direct anthropogenic aerosol forcing (all-sky, at TOA) in W/m^2 . Associated global averages are listed below the labels.

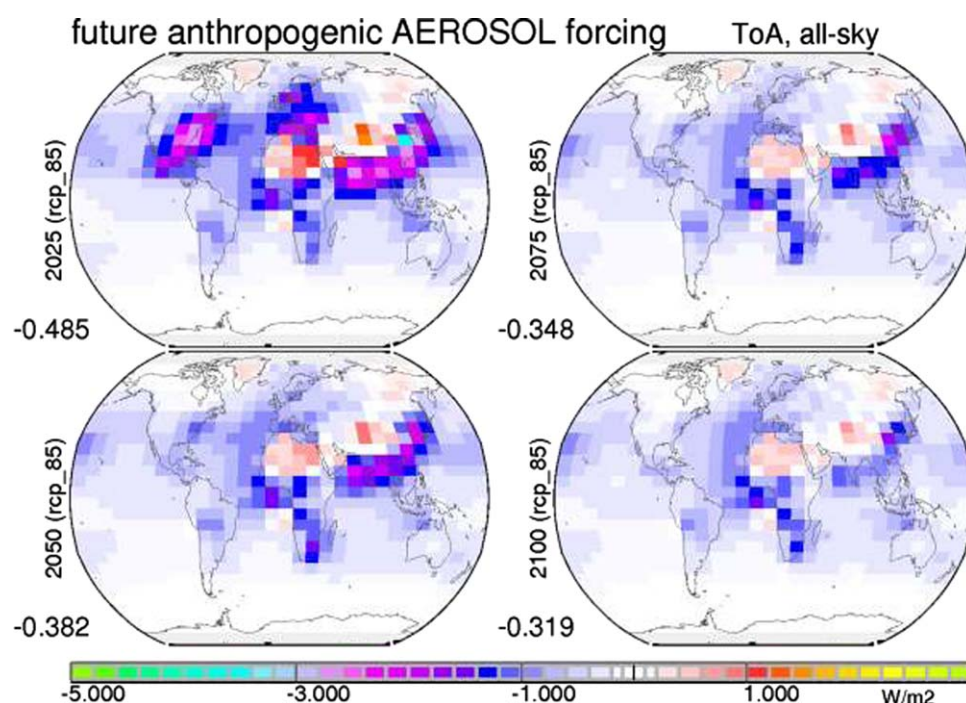


Figure 20. Annual average maps expected for future time slices (years 2025–2100) for the direct anthropogenic aerosol forcing (all-sky, at TOA) in W/m^2 , based on the IPCC 5AR rcp-8.5 future scenario. Future projections by alternate rcp-2.6 and rcp-4.5 emission scenarios (see associated AOD maps in Figure 13) yield similar results. Associated global averages are listed below the labels.

7. Sensitivities

[82] Several sensitivity tests were conducted to quantify the uncertainty of the (anthropogenic) aerosol forcing by modifying individual aerosol and environmental parameters according to their estimated uncertainty. Other sensitivities address individual contributions by sulfate and black carbon (BC) to the anthropogenic aerosol forcing and two simplifying assumptions, where in one case all aerosol absorption is removed and where in the other case all existing fine-mode aerosol at preindustrial times is ignored (such that anthropogenic aerosol at current conditions represents the entire fine mode).

7.1. Uncertainty Estimate

[83] The anthropogenic forcing estimates in this contribution have some built in uncertainties. Thus, sensitivities to four most influential input parameters are examined in terms of their impact on changes to the aerosol direct anthropogenic forcing for year 2000 conditions. Resulting forcing differences are presented in Figure 21 for four cases where (1) the aerosol is lifted by 1 km, (2) the solar surface albedo is increased by absolute 2%, (3) the fine-mode asymmetry-factor is increased by +0.03, and (4) the fine-mode aerosol absorption is increased, by increasing the AAOD by +0.003.

[84] The tendencies of all four test-cases happen all to be chosen such that the TOA cooling of -0.47 W/m^2 by anthropogenic for the year 2000 reference is reduced.

The lifting of aerosol places more absorbing aerosol above clouds so that the solar reflection of clouds is reduced, the increased surface albedo reduces the potential to cool by solar reflection and a larger asymmetry-factor reduces the solar reflection, because associated larger fine-mode sizes (for the same AOD) are less efficient solar reflectors. The solar backscatter is also reduced by increased absorption. Before adopting the impact of these deviations the realism of these assumptions is briefly examined.

[85] A 1 km uncertainty in altitude seems reasonable. Active remote sensing data by CALIPSO [Winker *et al.*, 2007] suggests in comparison to global modeling a lower altitude distribution for aerosol. However also, the ECHAM5-HAM, the model which defines the vertical aerosol profiles of the MAC-v1 climatology, has a relative low altitude distribution among global models. The relatively good agreement for the vertical aerosol distributions between CALIPSO and ECHAM5-HAM supports the assumption for a 1 km altitude error is sufficient.

[86] Similarly realistic is the assumed 2% error for the solar surface albedo, as there are usually issues with glint and whitecaps over oceans and issues in the representation of the solar spectral dependency and seasonality over continents. Sensitivity tests indicate that by ignoring the spectral dependence or seasonality the global anthropogenic forcing is less negative by 0.06 and 0.05, respectively.

[87] For the assumed aerosol size, a smaller aerosol fine-mode size is more likely, than a larger size which

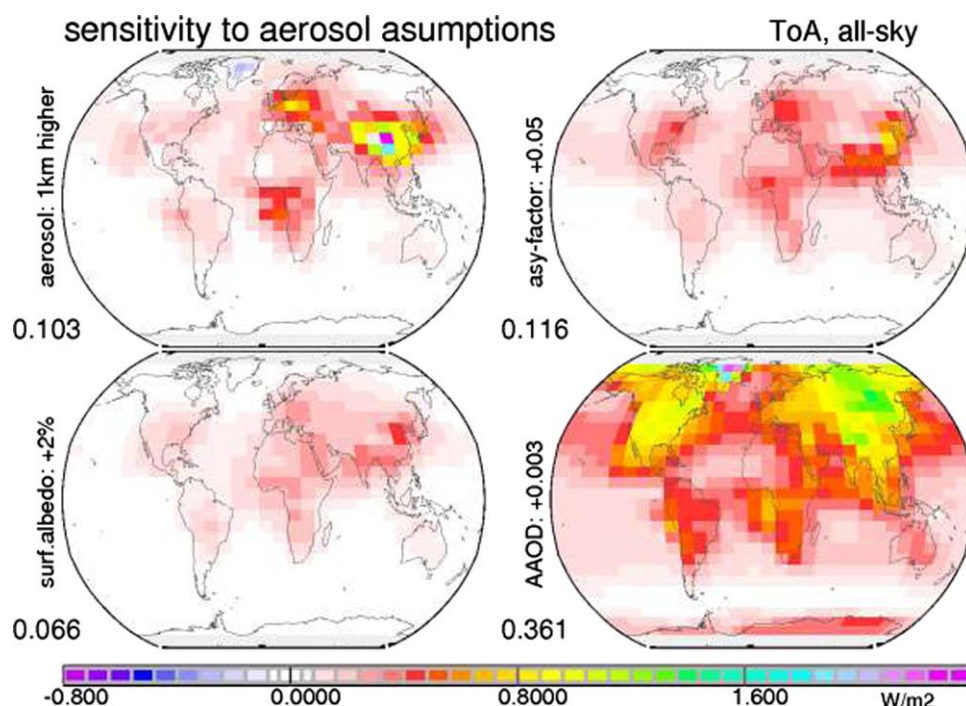


Figure 21. Differences to the annual average anthropogenic aerosol all-sky TOA forcing maps compared to the reference standard simulation in W/m^2 . Four different scenarios were explored: (top left) The aerosol altitude was raised by 1 km, (bottom left) an extra 2% is added to the solar surface albedo, (top right) the fine-mode aerosol size is increased by raising the fine-mode asymmetry-factor by 0.05, and (bottom right) the aerosol absorption is strengthened by adding 0.003 to the AAOD. Values below the labels indicate resulting differences to the standard annual global anthropogenic aerosol forcing of -0.47 W/m^2 .

was simulated with the increase to the solar asymmetry-factor (by 0.05). On the other hand for the tested forcing impacts an assumed larger aerosol size will be compensated by a smaller fine mode AOD, and vice versa. Thus, the overall impact of size change will be small. Still, with the rather general parameterization by using AnP_F , the assumed ASY_F values contain some uncertainty. Thus, an uncertainty of 0.025 to ASY_F is allowed which is half of the simulated sensitivity.

[88] Assumed changes to fine-mode absorption have the strongest impact. The concept behind this sensitivity test was to modify (here increase) the fine-mode absorption according to potential uncertainties in the AERONET inversion technique, because AERONET absorption serves as reference for the new climatology. Single AERONET inversion-based absorption retrievals have an uncertainty of about 0.01 (to AOD and similarly) to the absorption-AOD (O. Dubovik, 2012, private communication). As this is an uncertainty (and not a bias) and also as this uncertainty applies for a single inversion rather than for at least 10 inversions (which is the minimum number for a valid monthly average in this study) the AAOD uncertainty is reduced to 0.003.

[89] Combining all four errors (by assuming their randomness to each other), an overall uncertainty is determined. On a global annual basis, the direct aerosol forcing uncertainty is determined at $\pm 0.19 \text{ W/m}^2$ for the year 2000. Recalling an anthropogenic forcing of -0.47 W/m^2 for the year 2000 this corresponds to an

average error of 40%. Regional and seasonal details of this error are presented in Figure 22.

7.2. Anthropogenic Elements

[90] Four additional sensitivity tests were performed to address impacts of general assumptions and impacts by individual aerosol components to the anthropogenic aerosol forcing. Annual anthropogenic aerosol TOA forcing maps for these four scenarios at current (year 2000) conditions are presented in Figure 23 (and should be compared to the standard aerosol forcing maps in Figure 17 (top right)).

[91] An often applied approximation considers the entire fine-mode AOD as anthropogenic. This simplification ignores existing fine-mode AOD at preindustrial times, which may apply approximately for industrial regions of the Northern Hemisphere, but is a poor assumption for global assessments (see also Figure 11). The simulated global average anthropogenic TOA direct aerosol TOA forcing for this approximation is about -0.9 W/m^2 , thus, almost doubled over the reference case. This much stronger cooling is a bit surprising, because the added preindustrial AOD_F is only 50% of the anthropogenic AOD_F at current (year 2000) conditions. An explanation is by the presence of preindustrial AOD_F over lower reflecting surfaces.

[92] Aerosol absorption is an important modulator for the aerosol direct forcing. The simulations indicate that if anthropogenic aerosol would not absorb solar

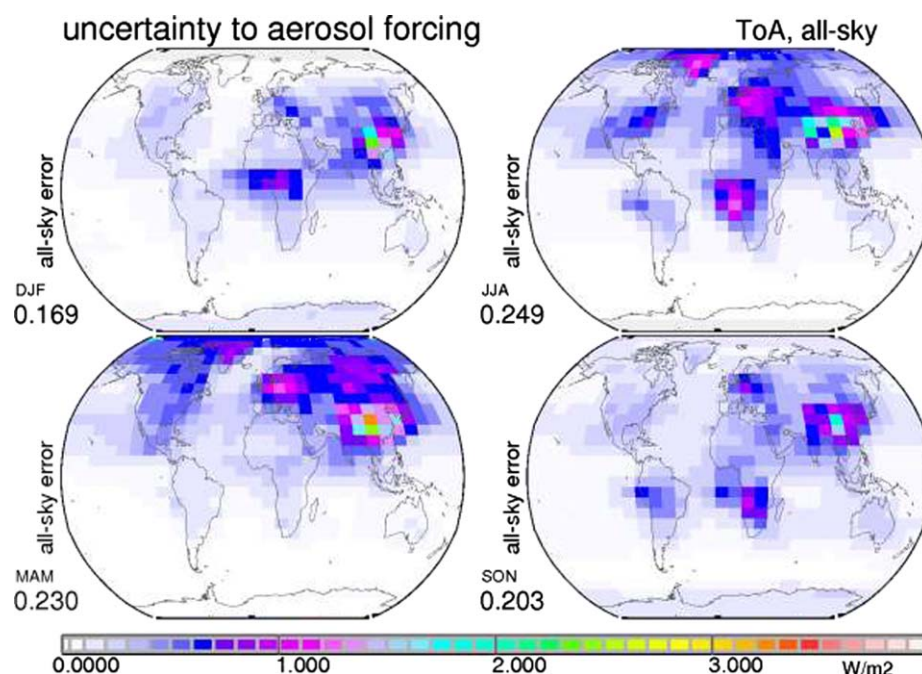


Figure 22. Seasonal maps for estimated uncertainties to current (year 2000) anthropogenic direct aerosol forcing (all-sky, at TOA) of Figure 17 in W/m^2 .

energy (to warm the atmosphere) anthropogenic aerosol TOA cooling would be near -1.1 W/m^2 rather than near -0.5 W/m^2 at current (year 2000) conditions. This demonstrates the importance to correctly quantify

absorption for anthropogenic aerosol and to accurately define the relative altitude between aerosol and clouds, with the potential of absorbing aerosol to dim unobstructed solar reflection by clouds to space.

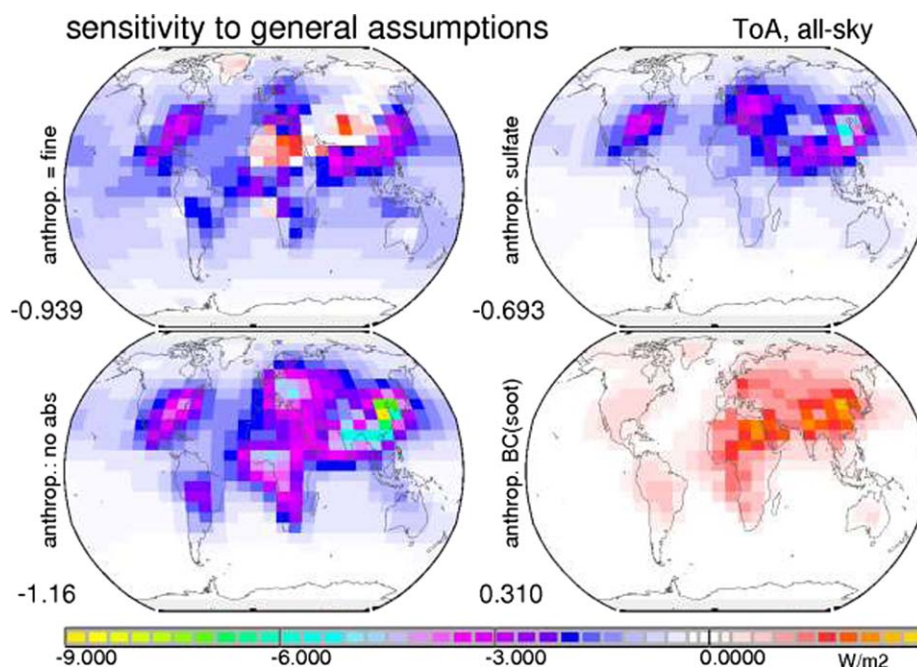


Figure 23. Annual average maps for the anthropogenic aerosol forcing (all-sky, at TOA) for current (year 2000) conditions in W/m^2 , associated with four specific sensitivity scenarios. (top left) The first test applies a simplification, in which the entire fine-mode aerosol is considered to be anthropogenic. (bottom left) The second test has all absorption removed from anthropogenic aerosol. (top right) The third test only considers the sulfate fine-mode anthropogenic impact and (bottom right) the fourth test only considers fine-mode absorbing impacts which are expressed via a BC AOD. Values below the labels indicate resulting direct aerosol forcing global averages.

Table 5. Summary of Global Average Mid-visible Aerosol Properties for AOD and SSA

Global Annual AOD at 550 nm		Global Annual SSA at 550 nm	
0.130	AOD – year 2000	0.958	SSA – year 2000
0.069	coarse mode AOD (radius > 0.5 μm)	0.982	coarse mode SSA (radius > 0.5 μm)
0.061	fine mode AOD (radius < 0.5 μm)	0.932	fine mode SSA (radius < 0.5 μm)
0.093	natural AOD	0.969	natural SSA
0.005	anthropogenic AOD – year 1900	0.930	anthropogenic SSA – year 1900
0.037	anthropogenic AOD – year 2000	0.927	anthropogenic SSA – year 2000
0.025	anthr. AOD – year 2000, over oceans	0.939	anthr. SSA – year 2000, over oceans
0.070	anthr. AOD – year 2000 over land	0.916	anthr. SSA – year 2000 over land
0.023	anthropogenic SSA – year 2100	0.930	anthropogenic SSA – year 2100

[93] Finally, contributions of two different aerosol components are estimated, that of scattering sulfate and that of strongly absorbing BC. To isolate sulfate within the fine-mode, model-ensemble based global monthly maps of sulfate AOD fine-mode fractions are applied along with (nonabsorbing) solar SSA values. To isolate BC, the entire fine-mode absorption (in terms of the midvisible AAOD) is projected on an absorption equivalent AOD for BC, by assuming a midvisible SSA of 0.28 for BC (based on MIE simulations for effective BC radii of 0.08 μm and a refractive index of $\text{RFI} = [1.7; 0.7]$).

[94] Sulfate only anthropogenic forcing is estimated at -0.7 W/m^2 and BC-only anthropogenic forcing is estimated at $+0.3 \text{ W/m}^2$. For the BC contribution, it should be noted that there is some uncertainty. There are arguments that BC forcing should be lower as fine-mode absorption from other aerosol types (such as organic carbon [OC]) was attributed to BC and there are arguments that BC forcing should be stronger, since the absorption by BC particles attached to coarse-mode aerosol was not included. Simulations which deduct from total absorption best estimates of the absorption by coarse-mode dust and by OC yield a (remaining) BC absorption that translates into an anthropogenic BC forcing of about $+0.45 \text{ W/m}^2$.

[95] The message from exploring aerosol component forcing contributions is that the component combined aerosol forcing is the result of larger contributions of opposite sign. This adds to the uncertainty of the anthropogenic aerosol direct forcing estimates.

8. Summary and Outlook

[96] The MAC-v1 climatology for tropospheric aerosol has been introduced. The climatology is comprised of monthly global (1°) maps for spectral dependent aerosol radiative properties. These maps permit a simple path to include impacts of tropospheric aerosol in climate simulations without a detailed prognostic aerosol treatment.

[97] Central to the climatology are midvisible aerosol column averages for AOD, SSA, and fine-mode AOD fraction (via AnP) obtained from a statistical merging of ground based sun/sky-photometer data onto central maps from AeroCom phase 1 global modeling. As major result of the merging submicron particles became smaller in size and more absorbing. These midvisible atmospheric column properties are extended to all

subspectral bands needed for radiative transfer modeling, by assuming that larger coarse-mode AOD over oceans as well as all coarse-mode AOD over continents is composed of dust. In addition, results from global modeling are applied to define (1) the local monthly vertical distribution of AOD and (2) the anthropogenic (fine mode) AOD as a function of time. Hereby, future AOD maps are tied to regional sulfur emission changes in future IPCC scenarios.

[98] Selected values for the (global, annual) aerosol column optical properties of the MAC-v1 aerosol climatology for midvisible AOD and SSA (see also Table 1) are shown in Table 5.

[99] The data can be interpreted such that about equal shares of AOD are contributed by the fine-mode and by the coarse-mode aerosol sizes. Currently (e.g., year 2000) there are also about equal shares of absorption (AAOD of about 0.003) by natural and anthropogenic aerosol and anthropogenic AOD is higher and more absorbing over continents than over oceans. Similar merging methods also involving AERONET statistics [Liu *et al.*, 2005; Chung *et al.*, 2005] are in good agreement for AOD data. The SSA or absorption values are less certain, but appear reasonable, although the simplification which keeps the SSA of anthropogenic aerosol constant over time should be revisited.

[100] The data of the MAC-v1 climatology were processed with an off-line radiative transfer code to yield maps for aerosol direct effects and aerosol forcing (the aerosol direct radiative effect at TOA over all-sky conditions). Selected results for the (global, annual) aerosol direct radiative effects (of Tables 4) are shown in Table 6.

[101] Interesting aspects are that on a global annual average basis the anthropogenic forcing is only about one third of the total aerosol radiative effect at the TOA and about equal, but opposite in sign, to the infrared greenhouse effect attributed to natural aerosol. While total aerosol radiative impacts are generally large enough to be detected under clear-sky conditions via solar broadband measurements from satellite or at the ground, anthropogenic measurements are illusive and involve assumptions on the preindustrial reference state on.

[102] The best estimate for the aerosol direct forcing is at about -0.5 W/m^2 with a $\pm 0.2 \text{ W/m}^2$ uncertainty. Compared to different model studies, this value is a bit more negative, but clearly within the uncertainty range of other estimates. Comparisons to global averages published in

Table 6. Summary of Aerosol Global Radiative Impacts

	Aerosol Radiative Impact Aspect
−1.6 W/m ²	total (short- and long-wave) aerosol direct rad. effect (TOA, all-sky)
−0.5 W/m ²	current (year 2000) anthropogenic aerosol direct forcing (TOA, all-sky)
2	factor overestimate, when not subtracting pre-industrial fine-mode
± 0.2 W/m ²	uncertainty to the anthropogenic aerosol direct forcing (TOA, all-sky)
+ 0.5 W/m ²	IR greenhouse attributed to (natural) aerosol
1.5 W/m ²	atmospheric solar warming by anthropogenic aerosol
3	factor larger atmos. divergence (cool, heat) over land than over oceans
−0.7 W/m ²	anthropogenic aerosol forcing by the sulfate component (TOA, all-sky)
+ 0.3 W/m ²	anthropogenic aerosol forcing by the soot component (TOA, all-sky)
−5 W/m ²	satellite observable solar aerosol rad. effect over oceans (TOA, clear)
−10 W/m ²	ground observable solar aerosol direct rad. effect over land (surf, clear)

other studies [Myhre *et al.*, 2009; Bellouin *et al.*, 2005; Bellouin *et al.*, 2008; Schulz *et al.*, 2006; Yu *et al.*, 2006; Chung *et al.*, 2005] are provided in Table 7. Overall there is good agreement. Except for one outlier [Chung *et al.*, 2005], due its unusually strong absorption (as already discussed when defining the anthropogenic term) there is good agreement for radiative effects not only at TOA but also for atmosphere and surface. In an effort to be complete, aerosol radiative effects (Table 4 and Figures 14–17) are not only offered for anthropogenic aerosol but also for total aerosol, hereby also distinguishing between solar only and combined solar and infrared impacts. In many aerosol representations (e.g., GEWEX SRB radiative fluxes) the infrared impact is often ignored, even though it offsets about one third of the solar impact.

[103] Such a summary of impacts by single values, however, does not do justice to temporal and especially spatial diversities of aerosol properties and their radiative impacts. Thus, an important element of this contribution is the presentation of associated maps. For instance, the average aerosol forcing is near -0.5 W/m^2 , but when exploring maps (see Figure 17) there are regions, where the aerosol forcing values is 10 times stronger and of both signs.

[104] An interesting aspect of the radiative forcing application is the temporal change for anthropogenic aerosol forcing. In Figure 24, simulated annual averages as function of time are compared between those for the entire globe as well as for the four major pollution regions of Europe, North America, South Asia, and East Asia. While the global average is expected to have reached its maximum around the year 2000, there is much more diversity on a regional basis. Regional aerosol cooling maxima in major pollution regions have already reached or will reach 2–4 times stronger values than the global maximum. Maxima for North America and Europe were already reached in the 1970s and 1980s and maxima for southern Asia and eastern Asia are projected for the 2010s.

[105] The presented aerosol radiative effects are based on simulation and projections with many assumptions. Although most assumptions in developing the climatology appear reasonable, there are elements that can and should be improved in newer versions of this climatology. Foremost, the density of surface-based reference data has increased. Aside from a better coverage by AERONET, there are in complementary data of other networks such as SkyNET [Aoki *et al.*, 2006] or GAW [Ingold *et al.*, 2001]. Also now many oceanic regions are covered through efforts of the Marine Aerosol Network [Smirnov *et al.*, 2009]. Thus, the ground-based reference has become much stronger. There is also room for improvement with respect to the merging (e.g., recursive schemes). Also modeling should deliver a better first guess value with advances in component treatment (e.g., nitrate, secondary organics). There also should be efforts to include information from (multiannual) satellite patterns, at least for the merging of AOD. Another element is ad hoc assumptions. Many of the parameterizations should be revisited, but at least verified by AERONET statistics. For instance, joint histograms have shown that size differences for the fine mode are not simply an ambient humidity issue, as assumed. And the fine-mode size is highly relevant for the determination of associated cloud condensation nuclei (CCN) which will be part of a future extension of the climatology. For better comparison to (satellite) data of a particular year, it is also desirable to consider the inclusion of natural (i.e., coarse mode) variability away from the

Table 7. Comparisons of MAC-v1 Values to Aerosol Direct Effects in Other Studies (in W/m²)

In W/m ²	MAC-v1	Myhre (2009)	Bellouin (2005/2008)	Schulz ^a (2006)	Yu (2006)	Chung (2005)
Anthropogenic TOA all-sky	−0.5	−0.35	−0.48	−0.20		−0.35
Anthropogenic atmosph. all-sky	1.4	1.51		1.55		3.15
Anthropogenic surface all-sky	−1.9	−1.86		−1.88		−3.50
Anthropogenic TOA clear-sky	−1.0	−1.07	−1.13			−1.08
Anthropogenic atmosph. clear-sky	1.5	1.52				3.42
Anthropogenic surface clear-sky	2.5	2.59				−4.44
Solar TOA clear-sky	−2.1		−1.9 ^b			
Solar atmosph. clear-sky	3.6		2.5 ^b			
Solar surface clear-sky	−5.7		−4.4 ^a			
TOA clear-sky ocean	−5.0				−5.5 ^b	

^aModel (A–G) average from published references by Liao and Seinfeld [2005], Reddy and Boucher [2004], Takemura *et al.* [2005], Kirkevåg and Iversen [2002], Jacobson [2001], Hansen *et al.* [2005], and Koch [2001].

^bObservation based estimates.

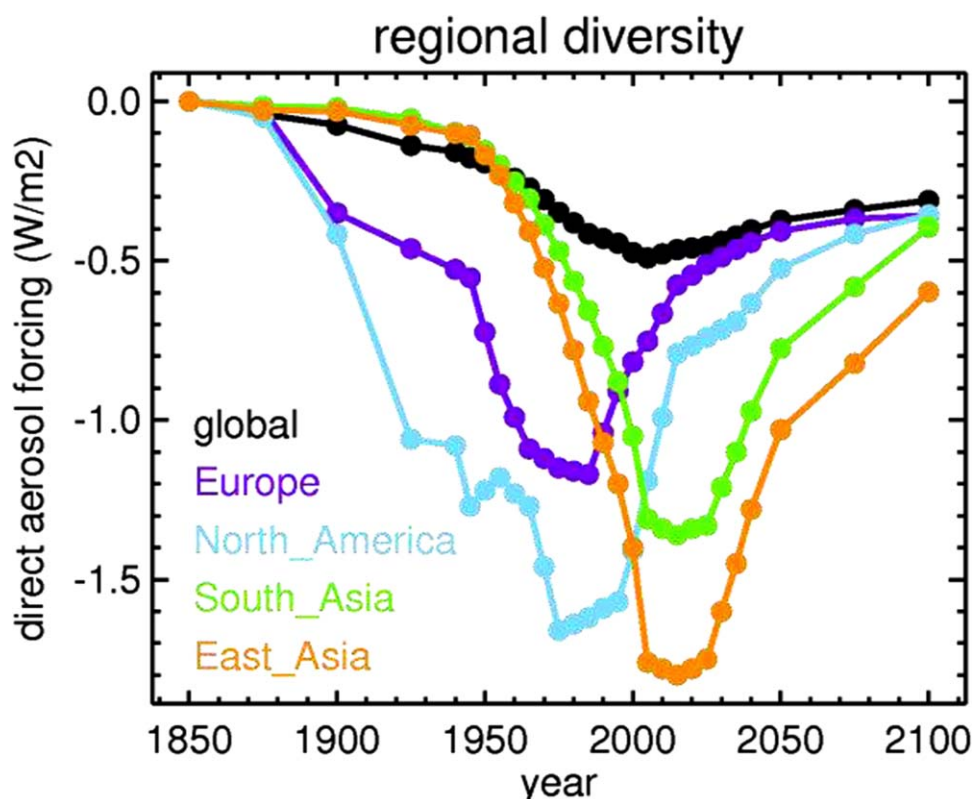


Figure 24. Simulated temporal changes in regional annual anthropogenic aerosol direct forcing (all-sky, at TOA) from preindustrial times (year 1850) into the future (up to year 2100). Estimates for future years are based on projected emissions of the RCP-8.5 scenario [Meinshausen *et al.*, 2011; Lamarque *et al.*, 2010]. Temporal changes for global averages are compared to temporal changes for Europe (25°N–65°N, 10°W–50°E), North America (10°N–55°N, 135°W–60°W), South Asia (5°N–35°N, 50°E–95°E), and East Asia (15°N–50°N, 95°E–160°E), following the regional definition of the HDAP [Yu *et al.*, 2013] experiments.

climatological average, possibly with a scaling of nudged (that is by meteorological data forced) simulations. Finally, there should be continuous attempts to replace parameterization or model simulations with sufficiently matured (multiannual) observational data, as the recently released CALIPSO version 3 data.

Appendix A: Radiative Transfer Aspects

[107] The applied radiative transfer code involves a two-stream method [Meador and Weaver, 1980] which is applied to 8 solar and 12 far-infrared spectral bands. Trace gas absorption of major trace gases (H_2O , O_3 , CO_2 , CO , N_2O , and CH_4) is represented by 50 solar and 70 infrared exponential terms. Atmospheric vertical profiles are approximated by 20 plane-parallel homogeneous atmospheric layers (with layer boundaries that were already mentioned in the discussions of aerosol vertical profiles). Default simulations use monthly maps at $1 \times 1^\circ$ (latitude/longitude) spatial resolution for input. Solar daily averages are based on weighted simulations at 10 different sun elevations.

[108] Aerosol radiative effects are not only a function of aerosol properties. The aerosol radiative effects also

depend on environmental parameters most prominently on (1) solar surface albedo, (2) cloud properties including cloud cover and altitude placement relative to aerosol, and (3) atmospheric state. Annual averages summarizing selected boundary data for the radiative transfer simulations are presented in Figure A1.

[109] For the solar surface albedo the assumed values over open oceans vary as function of the sun position between 3% (at overhead sun) to more than 20% (at low sun elevations) based a simple parameterization [Taylor *et al.*, 1996]: $\text{albedo (\%)} = 3.7 / [(1.1 \times (\mu_0^{1.4} + 0.15))]$, where μ_0 is the cosine of the solar zenith angle. Solar surface albedo data over continents are based on MODIS sensor data [Schaaf *et al.*, 2002] with different values for subspectral regions of the UV/visible (0.2–0.7 μm) and the near-IR (0.7–4.0 μm). Unfortunately, the MODIS data set has removed snow effects, when possible. To account for the higher reflection by these snow surface and also by sea ice, multiannual (1987–2007) monthly averages of SSM/I microwave satellite data [Basist *et al.*, 1996] for fractional snow and ice cover are combined with spectral albedo assumptions based on observational data [Brandt *et al.* 2005] (for snow: 90%

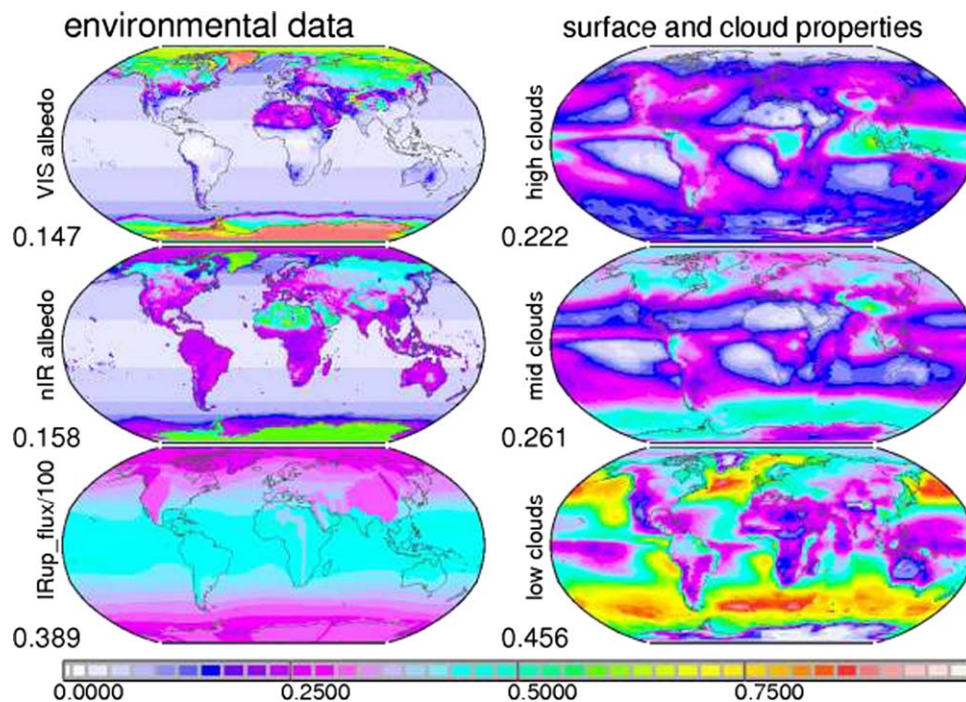


Figure A1. Annual average maps of assumed environmental data to (left column) surface properties and (right column) cloud cover properties. The left figure presents solar surface albedo data for the visible and the near-IR subspectral regions and the surface temperature related to upward IR flux from the surface (in $0.001 \times \text{W/m}^2$). Cloud properties, which are based on multiannual ISCCP data are here represented by the cloud cover assumptions for high-, mid-, and low-level clouds.

in the UV/visible region and 60% in the near-IR region; for sea ice: 65% in the UV/visible region and 25% in the near-IR region).

[110] Comparisons with solar surface albedo maps commonly applied in global modeling indicated that the resulting solar surface albedo values over continental region affected by snow cover are relatively high. This overestimate in solar surface albedo is mainly caused by a more recent finding (C. Schaaf, 2007, private communication) that snow was not completely removed in the MODIS data set and is now partially double counted. The assumption of a relative high solar surface albedo over continental regions affected by snow-cover

explains a relatively positive direct aerosol forcing in those regions.

[111] The cloud properties, which are required for all-sky conditions, use ISCCP multiannual (1984–1995) monthly cloud statistics for scene optical depths and cloud fractions in three (high, mid, and low) altitude regimes [Rossow *et al.*, 1993]. Since satellite sensors only detect clouds that are not obscured by higher altitude clouds, cloud cover for midlevel and low-level clouds are increased according to the unobserved fraction. In radiative transfer simulations at all-sky conditions a random cloud overlap accounts for all (8) cloud combinations involving high (6+ km), mid (3–6 km), and low (0–3 km) level clouds. Hereby, the ISCCP scene optical

Table B1. AERONET-sites With a q -Score of 3 (Excellent) and a r -Score of 3 (900 km)^a

AERONET q3/r3 (Site-Name)	Lon (deg)	Lat (deg)	Z (m)	Sun (Month)	Sun (Year)	Sky (Month)	Sky (Year)	Cat
Bermuda	295.30	32.37	10	12	7	11	4	Od2
Lanai	203.08	20.73	20	12	9	12	8	Od1
Midway_Island	182.62	28.22	0	12	4	12	4	O
Tahiti	210.38	−17.58	98	12	7	12	5	O

^aQualifying site names are listed in alphabetical order along with their location longitude (lon), latitude (lat), and altitude above sea level (z). For both direct attenuation (sun-) data and (sky-) inversion data products the number months covered (mon) and the number of different years contributing (y) are indicated (for the year 1996–2008 period). For valid monthly averages at minimum 50 samples for sun-data and at minimum 10 samples for sky-data are required. Only sites are listed in table with sun-data coverage for at least 5 months of the year. The category index (cat) addresses the site's dominant aerosol category (O, ocean; P, polluted; L, -land; D, dust; B, biomass; C, coastal; A, polar; M, mountain). The capital letter indicates the annual dominant type. The second small letter indicates a seasonal deviation in category dominance with its season (1, spring; 2, summer; 3, fall; and 4, winter).

Table B2. AERONET-Sites With q -Score of 3 (Excellent) and a r -Score of 2 (500 km)—as in Table B1

AERONET q3/r2 (Site-Name)	Lon (deg)	Lat (deg)	Z (m)	Sun (Month)	Sun (Year)	Sky (Mon)	Sky (Year)	Cat
Agoufou	358.52	15.35	305	12	4	12	3	D
Amsterdam_Island	77.57	−37.82	30	10	2	0	0	O
Azores	331.37	38.53	50	12	5	3	2	Od1
Bidi_Bahn	357.55	14.07	0	12	2	0	0	D
Bondoukou	356.25	11.85	0	12	3	0	0	Db4
Cape_San_Juan	294.38	18.38	15	11	2	0	0	D
Capo_Verde	337.07	16.73	60	12	12	12	9	D
Hornsund	15.55	77.00	0	7	2	3	2	A
Kaashidhoo	73.47	4.97	0	12	3	8	3	Op1
Kuujuarapik	282.20	55.30	0	7	3	1	1	L
Longyearbyen	15.65	78.22	30	5	2	1	2	A
MCO-Hanimaadhoo	73.18	6.78	0	6	2	4	1	Mp1
Mfuwe	31.93	−13.27	550	5	1	2	1	B
Mongu	23.15	−15.25	1107	12	12	12	11	B
Niabrara	259.98	42.77	730	5	2	3	2	L
Ouagadougou	358.60	12.20	290	12	8	12	7	Db4
Pickle_Lake	269.78	51.45	393	8	1	8	1	L
Prospect_Hill	295.30	32.37	63	11	1	4	1	L
Resolute_Bay	265.10	74.73	40	5	2	1	1	A
Rio_Branco	292.13	−9.97	212	12	6	9	4	B
Senanga	23.28	−16.12	1025	5	3	4	3	B
Thompson	262.15	55.80	218	7	9	6	5	L
Tomsk	85.05	56.48	130	11	5	10	4	L
Waskesiu	253.92	53.92	550	10	10	8	9	Lb2
Zambezi	23.12	−13.53	1040	6	3	4	3	B

Table B3. AERONET-Sites With q -Score of 3 (Excellent) and a r -Score of 1 (300 km)—as in Table B1

AERONET q3/r1 (Site-Name)	Lon (deg)	Lat (deg)	Z (m)	Sun (Month)	Sun (Year)	Sky (Month)	Sky (Year)	Cat
Abracos_Hill	297.63	−10.77	200	12	7	6	7	B
Al_Dhafra	54.55	24.25	40	6	1	3	1	D
Alta_Floresta	303.98	−9.92	175	12	11	9	10	B
Ames	266.22	42.02	1030	12	3	9	2	L
Anmyon	126.33	36.53	47	12	7	12	7	Cd1
Arica	289.68	−18.47	25	12	7	12	7	Pd1
BAHRAIN	50.62	26.22	25	12	3	12	3	Dp
BONDVILLE	271.63	40.05	212	12	11	12	11	L
Bac_Lieu	105.73	9.28	10	8	1	1	1	M
Bahrain	50.62	26.22	25	12	3	12	3	Dp
Banizoumbou	2.67	13.53	250	12	11	12	11	Db4
Belterra	305.05	−2.65	70	12	6	8	4	B
Bethlehem	28.33	−28.25	1709	12	2	11	2	Pb3
Blida	2.88	36.52	230	12	4	12	4	L
Bonanza_Creek	211.68	64.73	150	8	12	8	9	Ab2
Brasilia	312.10	−15.92	1100	10	3	5	3	B
Bratts_Lake	255.30	50.28	586	12	7	12	6	L
CARTEL	288.07	45.38	300	12	10	12	8	L
CART_SITE	262.52	36.62	318	11	2	7	2	L
CEILAP-BA	301.50	−34.57	10	12	8	12	6	P
CUIABA-MIRANDA	303.98	−15.73	210	12	5	7	5	B
Campo_Grande_SONDA	305.47	−20.43	677	12	4	11	3	B
Cart_Site	262.52	36.62	318	12	12	12	10	L
Chapais	284.02	49.82	381	8	1	7	1	L
Chequamegon	269.75	45.93	0	12	3	8	3	L
Concepcion	297.97	−16.13	500	5	2	5	2	B
Cuiaba	304.00	−15.50	250	8	3	5	2	B
Dahkla	344.05	23.72	12	12	2	12	2	D
Dakar	343.03	14.38	0	12	9	12	5	D
Dalanzadgad	104.42	43.58	1470	12	10	12	7	D
Dalma	52.33	24.50	0	6	1	4	1	D
Darwin	130.88	−12.42	29	8	2	8	2	C
Dhadnah	56.33	25.52	81	12	3	12	3	D
Djoungou	1.60	9.77	400	11	3	8	3	B
Dry_Tortugas	277.13	24.63	0	12	8	12	6	Od2

Table B3. (continued)

AERONET q3/r1 (Site-Name)	Lon (deg)	Lat (deg)	Z (m)	Sun (Month)	Sun (Year)	Sky (Month)	Sky (Year)	Cat
Dunedin	170.52	−45.87	43	12	2	4	1	L
Etosha_Pan	15.92	−19.17	1131	11	2	9	2	L
FLIN_FLON	258.32	54.67	305	6	2	4	2	L
FORTH_CRETE	25.28	35.33	20	12	4	12	4	C
GOA_INDIA	73.82	15.45	20	3	2	2	1	P
GSFC	283.17	38.98	87	12	14	12	14	P
Gosan_SNU	126.17	33.28	0	12	6	9	5	L
Halifax	296.42	44.63	65	12	5	12	5	C
Hamim	54.30	22.97	209	12	3	12	3	D
Helgoland	7.88	54.18	33	7	7	6	5	C
Howland	291.27	45.20	100	12	9	12	8	L
IER_Cinzana	354.07	13.28	285	12	3	12	3	D
IFT-Leipzig	12.43	51.35	125	12	6	10	6	L
Ilorin	4.33	8.32	350	12	9	10	5	Db4
Ji_Parana_SE	297.15	−10.93	218	6	1	4	1	B
Ji_Parana_UNIR	298.03	−10.88	100	5	1	3	1	B
KONZA_EDC	263.38	39.10	341	12	5	12	3	C
Kanpur	80.35	26.45	142	12	5	12	5	Pd1
Krasnoyarsk	92.77	55.98	202	8	2	5	2	L
LOS_FIEROS_98	299.07	−14.57	170	7	2	5	2	B
La_Parguera	292.97	17.97	12	12	6	11	4	C
Lake_Argyle	128.75	−16.12	150	12	4	12	4	L
Lampedusa	12.63	35.52	45	12	5	12	4	Cd2
Los_Alamos	253.67	35.87	2350	9	3	6	1	L
MD_Science_Center	283.38	39.28	15	12	9	12	9	P
Madison	270.58	43.07	326	6	2	0	0	L
Maricopa	248.03	33.07	360	12	6	12	6	L
Mexico_City	260.82	19.33	2268	12	8	11	7	P
Mezaira	53.78	23.15	204	5	1	5	1	D
Minsk	27.60	53.92	200	12	5	12	5	P
Moldova	28.82	47.00	205	12	8	12	8	P
Mukdahan	104.68	16.62	166	12	4	10	4	L
Mussafa	54.47	24.37	10	12	3	12	3	D
NSA_YJP_BOREAS	261.72	55.90	290	6	3	5	3	L
Perth	115.88	−32.02	0	6	2	1	1	C
Petrolina_SONDA	319.50	−9.38	370	10	2	1	1	O
Pimai	102.57	15.18	220	12	4	10	4	L
Rame_Head	355.85	50.37	0	7	2	1	1	C
Rottneist_Island	115.50	−32.00	70	12	4	11	2	O
SEDE_BOKER	34.78	30.85	480	12	10	12	10	D
SERC	283.50	38.88	10	12	8	12	6	C
SSA_YJP_BOREAS	255.35	53.67	490	6	3	5	2	L
Saih_Salam	55.32	24.83	84	5	1	5	1	D
Sevilleta	253.12	34.35	1477	12	12	12	11	L
Shelton	261.23	40.75	563	8	2	7	2	L
Shirahama	135.37	33.68	10	12	7	12	7	P
Sioux_Falls	263.37	43.73	500	12	9	12	8	L
Skukuza	31.58	−24.98	150	12	9	12	9	B
Solar_Village	46.42	24.92	650	12	8	12	8	D
TOULOUSE	1.48	43.57	150	7	2	3	2	P
Taihu	120.37	31.70	20	12	2	11	2	L
Tenosique	268.58	17.47	0	9	1	6	1	C
Tinga_Tingana	139.98	−28.98	38	12	5	12	5	L
Tombstone	249.95	31.73	1408	11	2	8	2	L
Toravere	26.47	58.27	70	10	5	10	5	L
Toulon	6.02	43.13	50	12	3	12	3	L
Toulouse	1.37	43.58	150	12	6	12	6	P
Trinidad_Head	235.85	41.05	107	9	2	1	1	L
Tuxtla_Gutierrez	266.85	16.75	0	9	1	6	1	L
USDA	283.12	39.03	50	10	2	10	2	L
Umm_Al_Quwain	55.67	25.53	20	5	1	5	1	D
XiangHe	116.97	39.75	36	12	4	11	4	L
Yakutsk	129.37	61.67	118	9	3	6	3	L
Yekaterinburg	59.53	57.03	300	10	3	6	1	L
Yulin	109.72	38.28	1080	9	2	9	2	L

Table B4. AERONET-Sites With q -Score of 3 (Excellent) and a r -Score of 0 (100 km)—as in Table B1

AERONET q3/r0 (Site-Name)	Lon (deg)	Lat (deg)	Z (m)	Sun (Month)	Sun (Year)	Sky (Month)	Sky (Year)	Cat
Aire_Adour	0.25	43.70	80	11	3	1	1	C
Avignon	4.88	43.93	32	12	8	12	8	P
BORDEAUX	359.42	44.78	40	12	3	11	3	P
BSRN_BAO_Boulder	254.98	40.03	1604	12	6	12	5	L
Bac_Giang	106.23	21.28	15	12	3	10	2	L
Barcelona	2.12	41.38	125	12	3	12	2	P
Beijing	116.38	39.98	92	12	6	12	6	P
Belsk	20.78	51.83	190	12	5	11	5	P
BillERICA	288.75	42.52	0	12	4	12	3	L
Brookhaven	287.12	40.87	33	12	4	11	3	C
Bucarest	26.52	44.45	44	11	2	6	2	P
CCNY	286.05	40.82	100	12	6	11	4	P
COVE	284.28	36.90	37	12	8	12	8	O
COVE_SEAPRISM	284.28	36.90	37	8	2	8	2	O
Cabauw	4.93	51.97	−1	10	2	7	1	C
Cabo_da_Roca	350.50	38.78	140	12	3	9	2	L
Cairo_EMA	31.28	30.08	70	12	2	12	2	P
Cairo_University	31.22	30.03	50	7	2	7	2	P
Canberra	149.12	−35.27	600	10	4	9	4	P
Carpentras	5.07	44.08	100	12	4	12	4	L
Chen-Kung_Univ	120.22	23.00	50	8	5	7	5	P
Chilbolton	358.57	51.13	88	11	2	4	1	L
Chulalongkorn	100.53	13.73	115	10	2	3	2	L
Columbia_SC	278.97	34.02	104	12	4	12	4	L
Corcoran	240.43	36.10	110	8	1	8	1	L
Cordoba-CETT	295.53	−31.52	730	12	8	12	8	P
Creteil	2.43	48.78	57	7	3	6	3	P
Crozet_Island	51.85	−46.43	221	6	1	0	0	C
Dunkerque	2.37	51.03	0	12	4	7	4	C
Egbert	280.25	44.23	264	12	9	12	7	L
Egbert_X	280.25	44.23	264	8	3	2	2	L
El_Arenosillo	353.27	37.10	0	12	7	12	7	C
Evora	352.08	38.57	293	12	4	12	4	L
Fontainebleau	2.68	48.42	85	12	5	8	5	P
Fresno	240.23	36.78	0	12	5	12	5	L
GISS	286.03	40.80	50	12	3	9	2	P
Gotland	18.95	57.92	10	10	6	8	4	C
Granada	356.38	37.17	680	8	2	7	1	L
Gustav_Dalen_Tower	17.47	58.58	25	6	2	5	2	C
Gwangju_K-JIST	126.50	35.13	60	12	3	9	2	L
HJAndrews	237.78	44.23	830	10	12	7	9	L
Hamburg	9.97	53.57	105	12	5	12	5	C
Harvard_Forest	287.82	42.53	322	5	2	3	1	L
Helsinki_Lighthouse	24.93	59.95	0	6	1	4	1	C
Hermosillo	249.03	29.08	237	11	2	5	2	L
Hong_Kong_PolyU	114.18	22.30	30	6	2	2	2	P
IMAA_Potenza	15.72	40.60	820	6	2	2	2	L
IMC_Oristano	8.50	39.92	10	12	4	12	4	C
IMS-METU-ERDEMLI	34.27	36.57	3	12	7	12	7	C
ISDGM_CNR	12.33	45.43	20	12	3	12	1	L
Inhaca	32.90	−26.03	73	8	3	8	2	B
Irkutsk	103.08	51.80	670	10	3	2	1	P
Karlsruhe	8.43	49.08	140	8	1	7	1	L
Kellogg_LTER	274.63	42.42	293	8	3	6	3	L
Kelowna	240.63	49.97	344	10	2	7	2	L
La_Crau	4.82	43.58	32	5	2	4	1	C
La_Jolla	242.75	32.87	115	12	7	12	6	C
Laegeren	8.35	47.48	735	11	4	7	4	L
Lecce_University	18.10	40.33	0	12	4	12	4	C
Lille	3.13	50.62	60	12	11	12	7	P
MISR-JPL	241.75	34.25	450	9	4	3	3	L
MVCO	289.45	41.30	10	10	2	6	2	L
Mainz	8.30	50.00	150	12	4	9	3	L
Messina	15.57	38.20	15	10	2	8	2	C
Missoula	245.92	46.92	1028	12	6	11	6	L
Modena	10.93	44.63	56	12	6	10	5	L
Monterey	238.13	36.58	50	12	3	11	3	C
Moscow_MSU_MO	37.52	55.70	192	11	6	10	6	P
Moss_Landing	238.22	36.78	20	5	1	3	1	C

Table B4. (continued)

AERONET q3/r0 (Site-Name)	Lon (deg)	Lat (deg)	Z (m)	Sun (Month)	Sun (Year)	Sky (Month)	Sky (Year)	Cat
Munich_Maisach	11.27	48.22	520	8	3	3	1	L
Nairobi	36.87	−1.33	1650	10	2	4	2	P
Nes_Ziona	34.78	31.92	40	12	7	12	7	D
Norfolk_State_Univ	283.73	36.85	20	7	1	6		C
Noto	137.13	37.33	200	8	2	3	2	L
OHP_OBSERVATOIRE	5.72	43.93	680	12	2	12	2	L
Oostende	2.92	51.22	23	12	5	10	5	C
Osaka	135.58	34.65	50	12	6	12	2	P
Oyster	284.07	37.28	8	12	4	9	4	C
Palaiseau	2.22	48.70	156	12	6	10	6	P
Palencia	355.48	41.98	750	12	4	12	4	L
Railroad_Valley	244.03	38.50	1435	9	4	7	4	L
Rimrock	243.02	46.48	824	12	6	12	6	L
Rogers_Dry_Lake	242.12	34.93	680	12	6	12	6	L
Rome_Tor_Vergata	12.65	41.83	130	12	6	0	0	P
SANTA_CRUZ	296.82	−17.80	442	12	8	5	3	B
SMHI	16.15	58.58	0	9	4	7	3	L
Saada	351.83	31.63	420	12	3	11	3	L
San_Nicolas	240.52	33.27	133	12	9	12	9	C
Santiago	289.28	−33.48	510	11	2	1	1	P
Saturn_Island	236.87	48.78	200	12	7	10	5	C
Seoul_SNU	126.95	37.47	116	10	4	8	2	P
Sopot	18.57	54.45	0	6	2	1	1	C
Stennis	270.38	30.37	20	12	5	12	5	C
THALA	8.68	35.55	1091	8	1	8	1	D
The_Hague	4.33	52.12	18	12	5	10	5	C
Toronto	280.53	43.97	300	6	5	1	1	P
Tucson	249.05	32.23	779	12	8	11	7	L
UCLA	241.55	34.07	131	12	5	12	4	P
UCSB	240.15	34.42	33	12	4	12	3	C
USDA-BARC	283.07	39.03	46	10	3	8	3	L
Univ_of_Houston	264.67	29.72	65	7	2	7	2	P
Ussuriysk	132.17	43.70	280	8	2	3	2	L
Venise	12.52	45.32	10	12	8	12	8	C
Villefranche	7.33	43.68	130	12	4	12	3	C
Walker_Branch	275.72	35.97	365	12	7	12	5	C
Wallops	284.53	37.93	10	12	11	12	11	C
Wits_University	28.22	−26.33	1775	6	2	0	0	P

Table B5. AERONET-Sites With q -Score of 2 (Moderate) and a r -Score of 3 (900 km)—as in Table B1

AERONET q2/r3 (Site-Name)	Lon (deg)	Lat (deg)	Z (m)	Sun (Month)	Sun (Year)	Sky (Month)	Sky (Year)
Ascension_Island	345.58	−7.98	30	12	9	11	6
Nauru	166.92	−0.52	7	12	8	2	1

Table B6. AERONET-Sites With q -Score of 2 (Moderate) and a r -Score of 2 (500 km)—as in Table B1

AERONET q2/r2 (Site-Name)	Lon (deg)	Lat (deg)	Z (m)	Sun (Month)	Sun (Year)	Sky (Month)	Sky (Year)
Balbina	300.52	−1.92	80	12	4	6	4
Guadeloup	298.50	16.33	0	11	2	5	2
MALE	73.53	4.18	2	12	4	2	1
Rio_Piedras	293.95	18.40	30	5	1	4	1

depth is distributed locally according to cloud cover and assumed relative ratios of 1 to 2 to 5 for optical depths of high-, mid-, and low-level clouds.

[112] Atmospheric state profiles such as temperature and trace gases were based on (seven) standard atmospheric profiles [Anderson *et al.*, 1986] for particular lati-

tude regimes (Arctic, midlatitudes, subtropics, and tropics) and for both summer and winter conditions. For months other than January and July, the summer and winter profiles were interpolated based on weights tied to changes in ISCCP near-surface temperature for that month and location.

Table B7. AERONET-Sites With q -Score of 2 (Moderate) and a r -Score of 1 (300 km)—as in Table B1

AERONET q2/r1 (Site-Name)	Lon (deg)	Lat (deg)	Z (m)	Sun (Month)	Sun (Year)	Sky (Month)	Sky (Year)
Barbados	300.50	13.17	0	12	5	2	1
Coleambally	146.07	−34.82	127	10	2	6	1
Dhabi	54.38	24.48	15	11	3	10	3
Jabiru	132.88	−12.67	30	12	6	10	4
Paddockwood	254.50	53.50	503	8	1	1	1
Surinam	304.80	5.80	0	12	4	6	3

Table B8. AERONET-Sites With q -Score of 2 (Moderate) and a r -Score of 0 (100 km)—as in Table B1

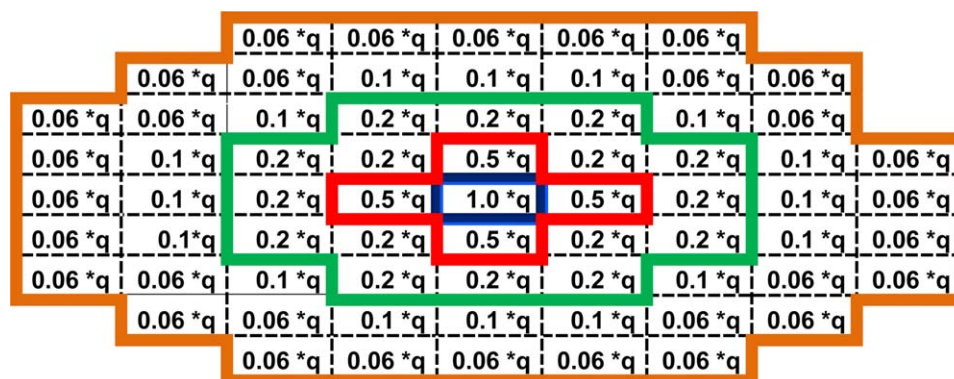
AERONET q2/r0 (Site-Name)	Lon (deg)	Lat (deg)	Z (m)	Sun (Month)	Sun (Year)	Sky (Month)	Sky (Year)
Albuquerque	253.47	35.05	1645	0	0	0	0
Barrow	203.33	71.32	0	7	5	5	3
Burtonsville	283.07	39.10	50	4	2	0	0
Ispra	8.63	45.80	235	12	10	12	10
Kejimikujik	294.72	44.38	154	11	3	0	0
Paris	2.33	48.87	50	12	3	6	1
Sao_Paulo	313.27	−23.57	865	12	6	12	6
Taipei_CWB	121.50	25.03	26	9	5	7	3

Table B9. AERONET-Sites With q -Score of 1 (Marginal) and a r -Score of 1 (300 km)—as in Table B1

AERONET q1/r1 (Site-Name)	Lon (deg)	Lat (deg)	Z (m)	Sun (Month)	Sun (Year)	Sky (Month)	Sky (Year)
Coconut_Island	202.22	21.43	0	12	0	10	5
Tukurui	310.32	−3.72	100	5	0	0	0

Table B10. AERONET-Sites With q -Score of 0 (Poor in Quality or Mountain Sites)—as in Table B1

AERONET q0 or r0 (Site-Name)	Lon (deg)	Lat (deg)	Z (m)	Sun (Month)	Sun (Year)	Sky (Month)	Sky (Year)
Big_Meadows	281.57	38.52	1082	5	2	2	1
ETNA	15.02	37.62	736	9	3	7	3
Jabal_Hafeet	55.78	24.07	1059	5	1	5	1
Mauna_Loa	204.42	19.53	3397	12	13	10	6
NCU_Taiwan	121.18	24.97	138	12	8	9	3
Red_Mountain_Pass	252.28	37.92	3368	10	2	0	0
TABLE_MOUNTAIN_CA	242.32	34.38	2200	12	3	12	2

**Figure B1.** Applied weights and spatial spreading of local data on a 1×1 deg lat/lon grid. Sites with a range score (r -score) of 0 are only applied locally (blue box). Sites with r -scores larger than 0 influence neighboring grid boxes, as illustrated for range scores of 1 (red interior), 2 (green interior), and 3 (brown interior). The products within each grid box indicate applicable weights, where the value indicates a distance decaying weight and q is the quality weight, which is 1.0, 0.66, 0.33, and 0.0 for quality-scores (q -scores) of 3, 2, 1, and 0, respectively. (Important ground-sites are listed by r -score and q -score combinations above in Tables B1–B10.)

Appendix B: Rating of AERONET Sites

[113] The importance of individual AERONET site data statistics differs in terms of regional representivity, data quality, and data volume. Thus, when combining monthly multiannual site statistics globally on a coarse regular grid, the strengths and weaknesses of individual AERONET sites should be considered. Thus, all AERONET sites are rated in terms of data quality (*q-score*) and domain range (*r-score*). These site scores were assigned by T. Eck (2009, personal communications). Tom Eck is a member of the AERONET staff at NASA-GFSC was involved in the deployment at many sites and is involved in regular monitoring activities. The *r(ange)*-scores range indicates a site's ability to represent its surrounding region. Data were stratified into four *r(ange)*-scores (3 = 900 km, 2 = 500 km, 3 = 300 km, and 0 = 100 km) and four *q(uality)*-scores (3 = excellent, 2 = moderate, 1 = marginal, and 0 = poor). Mountains peak sites were given a poor score (*q-score* = 0), because they are unable to represent their surrounding regions. Tables B1–B10 AERONET sites for same *r-score/q-score* combinations are listed in alphabetical order. Aside from site location data (i.e., longitude, latitude, and ground altitude) also information on volume of monthly statistics is given, by indicating the month and years covered (for the 1996–2008 periods), separately for sun data and sky data. Finally, among eight different categories (O, ocean; P, polluted; L, land; D, dust; B, biomass; C, coastal; A, polar; M, mountain) also the dominant aerosol type is indicated by the large letter in Tables B1–B4 (for AERONET sites with the highest quality score). An additional small letter indicates a different dominant aerosol type during a particular season, with the season indicated by a number (1, spring; 2, summer; 3, fall; and 4, winter).

[114] **Acknowledgments.** The AeroCom global modeling effort was essential to this study, as the model median provides the starting point for the new aerosol climatology. Thus, the work of all global modeling groups that contributed to AeroCom is acknowledged. Important remote sensing data were provided by many satellite retrievals groups and by the AERONET group at NASA-GSFC with particular assistance by Dave Giles and Ilya Slutsker. Also acknowledged is the support for Stefan Kinne by several, past and current, EU-projects, including MACC, MACC-2, EUCAARI, and ACTRIS. The aerosol properties described in this contribution are available on anonymous ftp://ftp-projects.zmaw.de cd aerocom/climatology/HACv1_2013/. (Contacting the first author is strongly recommended before pulling data from that ftp-site.)

References

Anderson, G., S. Clough, F. Kneizys, J. Chetwynd, and E. Shettle (1986), AFGL atmospheric constituent profiles (0.120 km), Rep. A371571, Air Force Geophys. Lab. Hanscom AFB, Mass.

Aoki, K. (2006), Aerosol optical characteristics in Asia from measurements of SKYNET sky radiometers, in *IRS 2004: Current Problems in Atmospheric Radiation*, edited by H. Fischer and B.-J. Sohn, pp. 311–313, A. Deepak.

Basist, A., D. Garrett, R. Ferraro, N. C. Grody, and K. Mitchell (1996), A comparison between visible and Microwave snow cover products derived from satellite observations, *J. Appl. Meteorol.*, **35**, 163–177.

Bauer, S. E., D. Koch, N. Unger, S. Metzger, D. Shindell, and D. Streets (2007), Nitrate aerosols today and in 2030: A global simulation including aerosols and tropospheric ozone, *Atmos. Chem. Phys.*, **7**, 5043–5059, doi:10.5194/acp-7-5043-2007.

Bellouin, N., O. Boucher, J. Haywood, and M. S. Reddy (2005), Global estimate of aerosol direct radiative forcing from satellite measurements, *Nature*, **438**, 1138–1141.

Bellouin, N., A. Jones, J. Haywood, and S. Christopher (2008), Updated estimate of aerosol direct radiative forcing from satellite observations and comparison against the Hadley Centre climate model, *J. Geophys. Res.*, **113**, D10205, doi:10.1029/2007JD009385.

Bellouin, N., J. Rae, A. Jones, C. Johnson, J. Haywood, and O. Boucher (2011), Aerosol forcing in the Climate Model Intercomparison Project (CMIP5) simulations by HadGEM2-ES and the role of ammonium nitrate, *J. Geophys. Res.*, **116**, D20206, doi:10.1029/2011JD016074.

Benedetti, A., et al. (2009), Aerosol analysis and forecast in the European Centre for Medium-Range Weather Forecasts Integrated Forecast System: 2. Data assimilation, *J. Geophys. Res.*, **114**, D13205, doi:10.1029/2008JD011115.

Bösenberg, J., et al. (2003), EARLINET: A European Aerosol Research LIdar NETwork to establish an aerosol climatology, Rep. 348, Max-Planck-Inst., Hamburg, Germany.

Brandt, R., S. G. Warren, A. P. Worby, and T. C. Grenfell (2005), Surface albedo of the Antarctic sea-ice zone, *J. Clim.*, **18**(17), 3606–3622.

Chin, M., P. Ginoux, S. Kinne, O. Torres, B. Holben, B. Duncan, R. Martin, J. Logan, A. Higurashi, and T. Nakajima (2002), Tropospheric aerosol optical thickness from the GOCART model and comparisons with satellite and sun photometer measurements, *J. Atmos. Sci.*, **59**, 461–483.

Chung, C. E., V. Ramanathan, D. Kim, and I. A. Podgorny (2005), Global anthropogenic aerosol direct forcing derived from satellite and ground-based observations, *J. Geophys. Res.*, **110**, D24207, doi:10.1029/2005JD006356.

Collins, W. D., P. J. Rasch, B. E. Eaton, B. V. Khattatov, J. F. Lamarque, and C. S. Zender (2001), Simulating aerosols using a chemical transport model with assimilation of satellite aerosol retrievals: Methodology for INDOEX, *J. Geophys. Res.*, **106**(D7), 7313–7336, doi:10.1029/2000JD900507.

Dave, J. V. (1968), Scattering of visible light by large water spheres, *Appl. Opt.*, **8**, 155–164.

Dentener, F., et al. (2006), Emissions of primary aerosol and precursor gases in the years 2000 and 1750, prescribed datasets for AeroCom, *Atmos. Chem. Phys.*, **6**, 4321–4344.

Dubovik, O., and M. D. King (2000), A flexible inversion algorithm for the retrieval of aerosol optical properties from Sun and sky radiance measurements, *J. Geophys. Res.*, **105**, 20,673–20,696.

Dubovik, O., A. Smirnov, B. N. Holben, M. D. King, Y. J. Kaufman, T. F. Eck, and I. Slutsker (2000), Accuracy assessments of aerosol optical properties retrieved from AERONET Sun and sky-radiance measurements, *J. Geophys. Res.*, **105**, 9791–9806.

Eck, T. F., B. N. Holben, J. S. Reid, O. Dubovik, A. Smirnov, N. T. O'Neill, I. Slutsker, and S. Kinne (1999), Wavelength dependence of the optical depth of biomass burning, urban, and desert dust aerosols, *J. Geophys. Res.*, **104**(D24), 31,333–31,349.

Hansen, J., et al. (2005), Efficacy of climate forcings, *J. Geophys. Res.*, **110**, D18104, doi:10.1029/2005JD005776.

Hess, M., P. Koepke, and I. Schult (1998), Optical properties of aerosols and clouds: The software package OPAC, *Bull. Am. Meteorol. Soc.*, **79**, 831–844.

Holben, B. N., et al. (1998), AERONET—A federated instrument network and data archive for aerosol characterization, *Remote Sens. Environ.*, **66**, 1–16.

Hsu, N. C., R. Gautam, A. M. Sayer, C. Bettenhausen, C. Li, M. J. Jeong, S. C. Tsay, and B. N. Holben (2012), Global and regional trends of aerosol optical depth over land and ocean using SeaWiFS measurements from 1997 to 2010, *Atmos. Chem. Phys.*, **12**, 8037–8053, doi:10.5194/acp-12-8037-2012.

Ingold, T., C. Mätzler, A. Heimo, N. Kämpfer, and A. Heimo (2001), Aerosol optical depth measurements by means of a sun-photometer network in Switzerland, *J. Geophys. Res.*, **106**(D21), 27,537–27,554.

Intergovernmental Panel on Climate Change (2007), Climate change, in *The Physical Science Basis, Contribution of Working Group I to the*

- Fourth Assessment Report of the Intergovernmental Panel on Climate Change*, edited by S. Solomon, et al., Cambridge Univ. Press, Cambridge, U. K.
- Jacobson, M. Z. (2001), Global direct radiative forcing due to multi-component anthropogenic and natural aerosols, *J. Geophys. Res.*, **106**(D2), 1551–1568.
- Kinne, S. (2009), Remote sensing data combinations-superior global maps for aerosol optical depth, in *Satellite Aerosol Remote Sensing Over Land*, edited by A. Kokhanovsky and G. de Leeuw, Springer, chapter 12, pp. 361–380.
- Kinne, S., et al. (2006), An AeroCom initial assessment—Optical properties in aerosol component modules of global models, *Atmos. Chem. Phys.*, **6**, 1–22.
- Kirkvæg, A., and T. Iversen (2002), Global direct radiative forcing by process-parameterized aerosol optical properties, *J. Geophys. Res.*, **107**(D20), 4433, doi:10.1029/2001JD000886.
- Koch, D. (2001), Transport and direct radiative forcing of carbonaceous and sulfate aerosols in the GISS GCM, *J. Geophys. Res.*, **106**(D17), 20,311–20,332.
- Koepeke, P., M. Hess, I. Schult, and E. P. Shettle (1997), Global Aerosol Data Set, Rep. 243, Max-Planck-Inst. für Meteorol., Hamburg, Germany, 44 pp.
- Koffi, B., et al. (2012), Application of the CALIOP layer product to evaluate the vertical distribution of aerosols estimated by global models: AeroCom phase I results, *J. Geophys. Res.*, **117**, D10201, doi:10.1029/2011JD016858.
- Lamarque, J.-F., et al. (2010), Historical (1850–2000) gridded anthropogenic and biomass burning emissions of reactive gases and aerosols: Methodology and application, *Atmos. Chem. Phys.*, **10**, 7017–7039, doi:10.5194/acp-10-7017-2010.
- Levy, R. C., L. A. Remer, R. G. Kleidman, S. Mattoo, C. Ichoku, R. Kahn, and T. F. Eck (2010), Global evaluation of the Collection 5 MODIS dark-target aerosol products over land, *Atmos. Chem. Phys.*, **10**, 10,399–10,420.
- Liao, H., and J. H. Seinfeld (2005), Global impacts of gas-phase chemistry-aerosol interactions on direct radiative forcing by anthropogenic aerosols and ozone, *J. Geophys. Res.*, **110**, D18208, doi:10.1029/2005JD005907.
- Liu, H., R. T. Pinker, and B. N. Holben (2005), A global view of aerosols from merged transport models, satellite, and ground observations, *J. Geophys. Res.*, **110**, D10S15, doi:10.1029/2004JD004695.
- Meador, W. E., and W. R. Weaver (1980), Two-stream approximation to radiative transfer in planetary atmospheres: A unified description of existing methods and new improvement, *J. Atmos. Sci.*, **37**, 630–643.
- Meinshausen, M., et al. (2011), The RCP greenhouse gas concentrations and their extension from 1765 to 2300, *Clim. Change*, **109**, 213–241, doi:10.1007/s10584-011-0156-z.
- Moss, R. H., et al. (2010), The next generation of scenarios for climate change research and assessment, *Nature*, **463**, 747–756.
- Myhre, G., et al. (2009), Modelled radiative forcing of the direct aerosol effect with multi-observation evaluation, *Atmos. Chem. Phys.*, **9**, 1365–1392.
- Nilsson, B. (1979), Meteorological influence on aerosol extinctions in the 0.2–40 μm wavelength range, *Appl. Opt.*, **18**, 3457–3473.
- Pappas, V., N. Hatzianastassiou, C. Papadimas, C. Matsoukas, S. Kinne, and I. Vardavas (2013), Spatio-temporal variability of global AeroCom aerosol optical depth and evaluation against MODIS and CALIOP data, *Atmos. Chem. Phys.*, [Epub ahead of print].
- Reddy, M. S., and O. Boucher (2004), A study of the global cycle of carbonaceous aerosols in the LMDZT general circulation model, *J. Geophys. Res.*, **109**, D14202, doi:10.1029/2003JD004048.
- Reddy, M. S., O. Boucher, N. Bellouin, M. Schulz, Y. Balkanski, J. L. Dufresne, and M. Pham (2005), Estimates of global multicomponent aerosol optical depth and direct radiative perturbation in the Laboratoire de Meteorologie Dynamique general circulation model, *J. Geophys. Res.*, **110**, D10S16, doi:10.1029/2004JD004757.
- Rossow, W., A. Walker, and C. Garder (1993), Comparison of ISCCP and other cloud amounts, *J. Clim.*, **6**, 2394–2418.
- Schaaf, C., et al. (2002), First observational BRDF, albedo and nadir reflectance from MODIS, *Remote Sens. Environ.*, **83**, 135–148.
- Schulz, M., et al. (2006), Radiative forcing by aerosols as derived from the AeroCom present-day and pre-industrial simulations, *Atmos. Chem. Phys.*, **6**, 5225–5346.
- Schutgens, N., M. Nakata, and T. Nakajima (2012), Estimating aerosol emissions by assimilating remote sensing observations into a global transport model, *Remote Sens.*, **4**, 3528–3543, doi:10.3390/rs4113528.
- Smirnov, A., et al. (2009), Maritime Aerosol Network as a component of Aerosol Robotic Network, *J. Geophys. Res.*, **114**, D06204, doi:10.1029/2008JD011257.
- Stevens, B., and S. Schwartz (2012), Observing and modeling Earth's energy flows, *Surv. Geophys.*, **33**, 779–816, doi:10.1007/s10712-012-9184-0.
- Stier, P., et al. (2005), The aerosol-climate model ECHAM5-HAM, *Atmos. Chem. Phys.*, **5**, 1125–1156.
- Sugimoto, N., I. Matsui, A. Shimizu, and T. Nishizawa (2008), Lidar network for monitoring Asian dust and air pollution aerosols, *IGARSS*, (2), 573–576.
- Takemura, T., T. Nozawa, S. Emori, T. Y. Nakajima, and T. Nakajima (2005), Simulation of climate response to aerosol direct and indirect effects with aerosol transport-radiation model, *J. Geophys. Res.*, **110**, D02202, doi:10.1029/2004JD005029.
- Tanre, D., J. F. Geleyn, and J. Slingo (1984), First results of the introduction of an advanced aerosol-radiation interaction in the ECMWF low resolution global model, in *Aerosols and Their Climatic Effects: Proceedings of the Meetings of Experts, Williamsburg, Virginia, 28–30 March 1983*, edited by H. E. Gerber and A. Deepak, pp. 133–177, A. Deepak, Hampton, Va.
- Taylor, J. P., J. M. Edwards, M. D. Glew, P. Hignett, and A. Slingo (1996), Studies with a flexible new radiation code. II: Comparisons with aircraft shortwave observations, *Q. J. R. Meteorol. Soc.*, **122**, 839–861.
- Textor, C., et al. (2006), Analysis and quantification of the diversities of aerosol life cycles within AeroCom, *Atmos. Chem. Phys.*, **6**, 1777–1811.
- Welton, E. J., J. R. Campbell, J. D. Spinhirne, and V. S. Scott (2001), Global monitoring of clouds and aerosols using a network of micro-pulse lidar systems, in *Lidar Remote Sensing for Industry and Environmental Monitoring*, edited by U. N. Singh, T. Itabe, and N. Sugimoto, Proc. SPIE, 4153, Lidar Remote Sensing for Industry and Environment, pp. 151–158.
- Winker, D. M., W. H. Hunt, and M. J. McGill (2007), Initial performance assessment of CALIOP, *Geophys. Res. Lett.*, **34**, L19803, doi:10.1029/2007GL030135.
- Yu, H., et al. (2006), A review of measurement-based assessments of the aerosol direct radiative effect and forcing, *Atmos. Chem. Phys.*, **6**, 613–666, doi:10.5194/acp-6-613-2006.
- Yu, H., et al. (2013), A HTAP multi-model assessment of the influence of regional anthropogenic emission reductions on aerosol direct radiative forcing and the role of intercontinental transport, *J. Geophys. Res.*, **118**, D018148, doi:10.1029/2012JD018148.